The Astronomical Journal, 148:108 (17pp), 2014 December doi:10.1088/0004-6256/148/6/108

A TECHNIQUE TO DERIVE IMPROVED PROPER MOTIONS FOR *KEPLER* OBJECTS OF INTEREST*

G. Fritz Benedict[1], Angelle M. Tanner[2], Phillip A. Cargile[3,4], and David R. Ciardi[5]
[1] McDonald Observatory, University of Texas, Austin, TX 78712, USA; fritz@astro.as.utexas.edu
[2] Department of Physics and Astronomy, Mississippi State University, Starkville, MS 39762, USA
[3] Department of Physics and Astronomy, Vanderbilt University, Nashville, TN 37235, USA
[4] Harvard-Smithsonian Center for Astrophysics, 60 Garden Street, Cambridge, MA 02138, USA
[5] NASA Exoplanet Science Institute, Caltech, Pasadena, CA 91125, USA
Received 2014 June 20; accepted 2014 August 15; published 2014 October 30

ABSTRACT

We outline an approach yielding proper motions with higher precision than exists in present catalogs for a sample of stars in the *Kepler* field. To increase proper-motion precision, we combine first-moment centroids of *Kepler* pixel data from a single season with existing catalog positions and proper motions. We use this astrometry to produce improved reduced-proper-motion diagrams, analogous to a Hertzsprung–Russell (H-R) diagram, for stars identified as *Kepler* objects of interest. The more precise the relative proper motions, the better the discrimination between stellar luminosity classes. Using UCAC4 and PPMXL epoch 2000 positions (and proper motions from those catalogs as quasi-Bayesian priors), astrometry for a single test Channel (21) and Season (0) spanning 2 yr yields proper motions with an average per-coordinate proper-motion error of 1.0 mas yr^{-1}, which is over a factor of three better than existing catalogs. We apply a mapping between a reduced-proper-motion diagram and an H-R diagram, both constructed using *Hubble Space Telescope* parallaxes and proper motions, to estimate *Kepler* object of interest *K*-band absolute magnitudes. The techniques discussed apply to any future small-field astrometry as well as to the rest of the *Kepler* field.

Key words: astrometry – planetary systems – proper motions – stars: distances

Online-only material: color figures

1. INTRODUCTION

Astrometric precision, ϵ, in the absence of systematic error, is proportional to $N^{-1/2}$, where N is the number of observations (van Altena 2013). Theoretically, averaging the existing vast quantity of *Kepler* data might allow us to approach *Hubble Space Telescope* (*HST*)/Fine Guidance Sensor astrometric precision, 1 ms of arc per observation. While *Kepler* was never designed to be an astrometric instrument, and despite significant astrometric systematics and the challenge of fat pixels (3.″9757 pixel^{-1}), we can reach a particular goal; higher-precision proper motions for *Kepler* objects of interest (KOIs) from *Kepler* data. Additionally, these techniques might be useful to future astrometric users of, for example, the Large Synoptic Survey Telescope (Ivezic et al. 2008), when they require the highest-possible astrometric precision for targets of interest contained on a single CCD in the focal plane. Finally, proper-motion measurements from any *Kepler* extended mission might benefit from the application of these techniques.

In transit work, it is useful to know the luminosity class of a host star when estimating the size of the companion. This requires a distance, ideally provided by a measurement of the parallax. With simple centroiding unaware of point-spread function (PSF) structure, the season-to-season *Kepler* astrometry required for parallaxes presently yields positions with average errors exceeding 100 milliarcseconds (mas), which is insufficient for parallaxes (Section 4.3). However, distance is a desirable piece of information. Reduced-proper-motion (RPM) diagrams may provide an alternative distance estimate. The concept is simple: proper motion becomes a proxy for distance (Stromberg 1939; Gould & Morgan 2003; Gould 2004). Statistically, the closer any star is to us, the more likely it is to have a larger proper motion. The RPM diagram consists of the proper motion converted to a magnitude-like parameter plotted against the color. The RPM diagram is thus analogous to a Hertzsprung–Russell (H-R) diagram. While some nearby stars might have low proper motions, giant and dwarf stars typically are separable. The more precise the proper motions, the better the discrimination between the stellar luminosity classes.

In the following sections, we describe our approach yielding improved placement within an RPM for any *Kepler* target of interest. In Section 2, we outline the utility of RPM diagrams, including a calibration to absolute magnitude derived from *HST* astrometry. In Section 3, we discuss *Kepler* data acquisition and reduction. We present the results of a number of tests providing insight into the many difficulties associated with *Kepler* astrometry in Section 4. We describe the modeling and proper-motion results for our selected *Kepler* test field in Section 5. We compare our improved RPM with that previously derived from existing astrometric catalogs (Section 5.8), and discuss the astrophysical ramifications of our estimated absolute magnitudes for the over 60 KOI's in our test field (Section 6). We summarize our findings in Section 7.

2. A CALIBRATED RPM DIAGRAM

In past *HST* astrometric investigations (e.g., Benedict et al. 2011; McArthur et al. 2010), the RPM was used to confirm the spectrophotometric stellar spectral types and luminosity classes of reference stars. Their estimated parallaxes are input to the model as observations with associated errors. To minimize absorption effects, *HST* astrometric investigations use $H_K(0) = K(0) + 5\log(\mu)$ for the magnitude-like parameter and $(J-K)_0$ for the color, where the K magnitudes and $(J-K)$ colors (from the Two Micron All Sky Survey (2MASS); Skrutskie et al. 2006) have been corrected for interstellar extinction. For all of our RPMs, we use the vector length proper motion, $\mu = (\mu_{\rm RA}^2 + \mu_{\rm DEC}^2)^{1/2}$.

* Based on observations made with the NASA *Kepler* Telescope.

Table 1
HST $M_K(0)$ and $H_K(0)$

No.	ID	$m-M$	$M_K(0)$	SpT	μ_T [a]	K_0	$(J-K)_0$	$H_K(0)$	References [b]
1	HD 213307	7.19	−0.86	B7IV	21.82 ± 0.42	6.32	−0.12	−1.98 ± 0.05	B02
2	υ AND	0.66	2.20	F8 IV–V	419.26 0.14	2.86	0.32	0.97 0.03	M10
3	HD 136118	3.59	2.00	F9V	126.31 1.20	5.60	0.34	1.11 0.03	Mr10
4	HD 33636	2.24	3.32	G0V	220.90 0.40	5.56	0.34	2.28 0.03	Ba07
5	HD 38529	3.00	1.22	G4IV	162.31 0.11	4.22	0.68	0.27 0.03	B10
6	vA 472	3.32	3.69	G5 V	104.69 0.21	7.00	0.50	2.10 0.03	M11
7	55 Cnc	0.49	3.49	G8V	539.24 1.18	3.98	0.70	2.64 0.03	SIMBAD
8	δ Cep	7.19	−4.91	F5Iab:	17.40 0.70	2.28	0.52	−6.51 0.09	B07
9	vA 645	3.79	4.11	K0V	101.81 0.76	7.90	0.77	2.93 0.03	M11
10	HD 128311	1.09	3.99	K1.5V	323.57 0.35	5.08	0.53	2.63 0.03	M13
11	γ Cep	0.67	0.37	K1IV	189.20 0.50	1.04	0.62	−2.58 0.03	B13
12	vA 627	3.31	3.86	K2 V	110.28 0.05	7.17	0.56	2.38 0.03	M11
13	ϵ Eri	−2.47	4.24	K2V	976.54 0.10	1.78	0.45	1.72 0.03	B06
14	vA 310	3.43	4.09	K5 V	114.44 0.27	7.52	0.63	2.82 0.03	M11
15	vA 548	3.39	4.13	K5 V	105.74 0.01	7.52	0.71	2.64 0.03	M11
16	vA 622	3.09	5.13	K7V	107.28 0.05	8.22	0.84	3.38 0.03	M11
17	vA 383	3.35	5.01	M1V	102.60 0.32	8.36	0.91	3.42 0.03	M11
18	Feige 24	4.17	6.38	M2V/WD	71.10 0.60	10.55	0.69	4.81 0.03	B00a
19	GJ 791.2	−0.26	7.57	M4.5V	678.80 0.40	7.31	0.92	6.47 0.03	B00b
20	Barnard	−3.68	8.21	M4Ve	10370.00 0.30	4.52	0.72	9.60 0.03	B99
21	Proxima	−4.43	8.81	M5Ve	3851.70 0.10	4.38	0.97	7.31 0.03	B99
22	TV Col	7.84	4.84	WD	27.72 0.22	12.68	0.49	4.89 0.03	M01
23	DeHt5	7.69	7.84	WD	21.93 0.12	15.53	−0.07	7.24 0.03	B09
24	N7293	6.67	7.87	WD	38.99 0.24	14.54	−0.23	7.49 0.03	B09
25	N6853	8.04	2.54	WD	8.70 0.11	10.58	1.13	0.27 0.04	B09
26	A31	8.97	6.69	WD	10.49 0.13	15.66	0.25	5.77 0.04	B09
27	V603 Aql	7.20	4.12	CNe	15.71 0.19	11.32	0.31	2.30 0.04	H13
28	DQ Her	8.06	5.00	CNe	13.47 0.32	13.06	0.46	3.70 0.06	H13
29	RR Pic	8.71	3.54	CNe	5.21 0.36	12.25	0.18	0.83 0.15	H13
30	HP Lib	6.47	7.35	WD	33.59 1.54	13.82	−0.12	6.45 0.10	R07
31	CR Boo	7.64	8.59	WD	38.80 1.78	16.23	−1.52	9.17 0.10	R07
32	V803 Cen	7.70	6.12	WD	9.94 2.98	13.82	−0.10	3.81 0.65	R07
33	ℓ Car	8.56	−7.55	G3Ib	15.20 0.50	0.99	0.55	−8.10 0.08	B07
34	ζ Gem	7.81	−5.73	G0Ibv	6.20 0.50	2.13	0.23	−8.91 0.18	B07
35	β Dor	7.50	−5.62	F6Ia	12.70 0.80	2.06	0.48	−7.42 0.14	B07
36	FF Aql	7.79	−4.39	F6Ib	7.90 0.80	3.45	0.40	−7.06 0.22	B07
37	RT Aur	8.15	−4.25	F8Ibv	15.00 0.40	3.90	0.28	−5.22 0.06	B07
38	κ Pav	6.29	−3.52	F5Ib-II:	18.10 0.10	2.71	0.62	−6.00 0.03	B11
39	VY Pyx	6.00	−0.26	F4III	31.80 0.20	5.63	0.33	−1.86 0.03	B11
40	P3179	5.65	3.02	G0V:	50.36 0.40	8.67	0.35	2.18 0.03	S05
41	P3063	5.65	4.68	K6V:	45.30 0.50	10.33	0.82	3.61 0.04	S05
42	P3030	5.65	4.97	K9V:	43.20 0.50	10.62	0.83	3.79 0.04	S05

Notes.
[a] $\mu_T = (\mu_{RA}^2 + \mu_{DEC}^2)^{1/2}$ in mas yr^{-1}.
[b] B99 = Benedict et al. (1999), B00a = Benedict et al. (2000a), B00b = Benedict et al. (2000b), B02 = Benedict et al. (2002), B06 = Benedict et al. (2006), B07 = Benedict et al. (2007), B09 = Benedict et al. (2009), B11 = Benedict et al. (2011), Ba07 = Bean et al. (2007), H13 = Harrison et al. (2013), Mr10 = Martioli et al. (2010), M01 = McArthur et al. (2001), M11 = McArthur et al. (2011), R07 = Roelofs et al. (2007), S05 = Soderblom et al. (2005).

Compared to *Hipparcos*, *HST* has produced only a small number of parallaxes and proper motions (Benedict et al. 1999, 2000a, 2000b, 2002, 2006, 2007, 2009, 2011; Harrison et al. 2013; McArthur et al. 2001, 2010, 2011, 2014; Roelofs et al. 2007), but with higher precision. Parallax and proper-motion results for 42 stars with *HST* proper-motion and parallax measures are collected in Table 1. Average parallax errors are 0.2 mas. Average proper-motion errors are 0.4 mas yr^{-1}. In Figure 1, we compare an H-R diagram and an RPM diagram constructed with *HST* parallax and proper-motion results for the targets listed in Table 1. Conspicuously absent from the RPM diagram are the RR Lyr results from Benedict et al. (2011) with their large proper motions due to their Halo Pop II identification. Lines plotted on the H-R diagram show predicted loci for 10 Gyr age solar metallicity stars and 3 Gyr age metal-poor stars from Dartmouth Stellar Evolution models (Dotter et al. 2008). These ages and metallicities encompass the majority of what might be expected from a random sampling of stars in our Galaxy.

Even though these targets are scattered all over the sky and range from planetary nebula central stars to Cepheid variables, the similarity between the H-R and RPM diagrams is striking. In Figure 2, we plot the extinction-corrected *K*-band absolute magnitude derived from *HST* parallaxes against the magnitude-like parameter $H_K(0)$. The resulting scatter, 0.7 mag rms, suggests that precise proper motion is a good enough proxy for distance to allow us to assign a luminosity class.

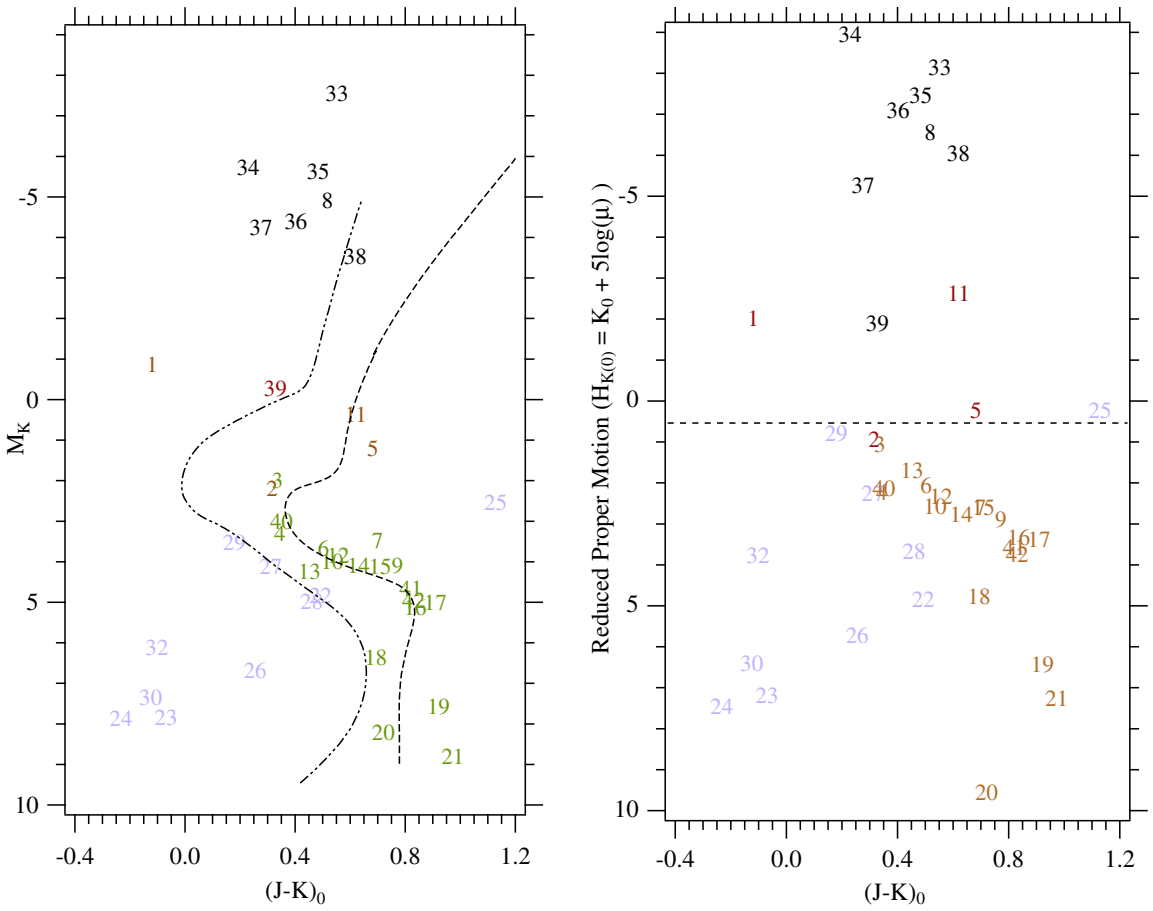

Figure 1. Left: Hertzsprung–Russell (H-R) diagram absolute magnitude $M_K(0)$ vs. $(J-K)_0$, both corrected for interstellar extinction. Plotted lines show predicted loci for 10 Gyr age solar metallicity stars (- - -) and 3 Gyr age metal-poor ([Fe/H] = −2.5) stars (-···-) from Dartmouth Stellar Evolution models (Dotter et al. 2008). Right: RPM diagram, same targets plotted. Horizontal lines separate main sequence and sub-giants, and giants and super-giants. Star numbers are from Table 1. The color coding denotes main-sequence stars (red), white dwarfs (blue), and super-giants (black).

(A color version of this figure is available in the online journal.)

Note that while this calibration is produced with proper motions sampling much of the celestial sphere, the H-R diagram and RPM main sequences are defined almost exclusively by stars belonging to the Hyades and Pleiades clusters. This may become an issue when we attempt to apply the calibration to a small piece of the sky in a different location. Both the calibration sources and a random *Kepler* field have systematic proper motions due to galactic rotation (see van Leeuwen 2007, Section 6.1.5), which may require some correction.

3. *KEPLER* OBSERVATIONS AND DATA REDUCTION

The primary mission of the *Kepler* spacecraft is high-precision photometry which can be used to discover transiting planets. *Kepler* rotates about the boresight once every 90 days to maximize solar panel illumination. Each such pointing is identified by a season number; 0–3. Each 90 day period is identified by a quarter number; 1–17. The CCDs in the *Kepler* focal plane are identified by a channel number; 1–84. Our goal is to produce an astrometric reference frame across a given *Kepler* channel containing KOIs of interest, with the end product being KOI proper motions which can be used to populate an RPM.

3.1. Star Data

The *Kepler* telescope trails the Earth in a Sun-centered orbit. Details on the photometric performance and focal plane array can be found in Borucki et al. (2010) and Caldwell et al. (2010a). The following explorations restrict themselves to the so-called long-cadence data where each subsection containing a star of interest in the array is read out once every 30 minutes. These subsections of the *Kepler* field of view (FOV; hereafter, postage stamps) range from 4×5 pixels for fainter stars to larger than 8×8 pixels for brighter stars. *Kepler* pixels are a little less than 4″ on a side. Targets observed with long cadence generate approximately 4700 postage stamps per star per quarter.

We obtained our *Kepler* data from the Space Telescope Science Institute Multimission Archive (MAST). These data include both pipelined positions (the *_llc.fits files, where "*" is a global replacement marker) and postage stamp image data (the *_lpd-targ.fits files). The *Kepler* Archive Manual (Fraquelli & Thompson 2012) greatly assisted us with any access issues.

3.2. Positions from Kepler Image Data

Positions used in this paper are generated from the *Kepler* postage stamp image data using a simple first-moment centering algorithm. We calculate

$$MOM\_CENTR\_X = \sum i * z / \sum i, \quad (1)$$

$$MOM\_CENTR\_Y = \sum j * z / \sum j, \quad (2)$$

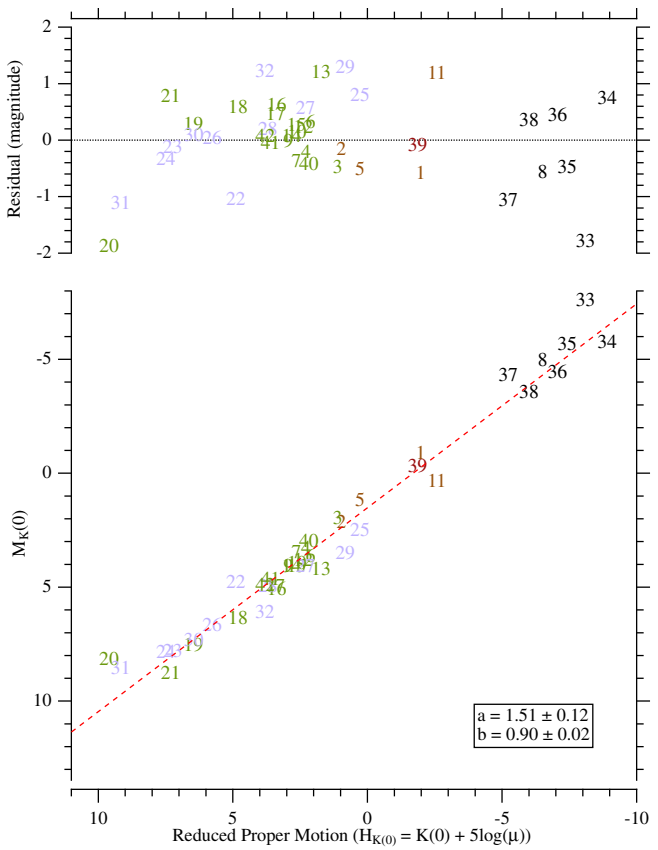

Figure 2. Linear mapping between $M_K(0)$ and $H_K(0)$ using *HST* parallaxes and proper motions for targets scattered over the entire sky. rms residual is 0.7 mag. The linear fit ($M_K(0) = a + b\,H_K(0)$) coefficient errors are 1σ. Stellar classifications range from white dwarfs to Cepheids, as listed in Table 1.

(A color version of this figure is available in the online journal.)

where $z = \mathrm{flux}(i, j)$ are the flux count values for each *Kepler* pixel within the postage stamp. To generate positions from the optimal aperture, any z value not in the optimal aperture is set to zero. To reduce the computational load and to smooth out high-frequency positional variations, normal points (NPs) are formed by averaging the x and y positions for a specified time span. The tests and results reported herein are based on nine day NPs. We also only use data within an optimal aperture for each star defined by the *Kepler* team. We provide an example of an optimal aperture for a star with *Kepler* identification number KID = 7031732 in Figure 3. There are positional corrections tabulated in the MAST data products, e.g., POS_CORR1. These corrections report the size of the differential velocity aberration, pointing drift, and thermal effects applicable to the region of sky recorded in the file. These corrections are applied to our derived centroids. The final positions used in the test are corrected using the MAST position correction values, e.g., XY_CORR = MOM_CENTR_XY - POS_CORR_XY. We calculate the standard deviation of each NP along each axis for each star. The average standard deviation of these NP is typically on the order of 1 mas, demonstrating exceptional astrometric stability within each postage stamp. However, this small, formal random error is a significant underestimation of the total star-to-star astrometric quality, as we will see below in Section 4.1.

We explored utilizing PSF fitting methods to extract positions. That approach did not resolve the issue of poor astrometric performance over multiple quarters (see Section 4.3 below). PSF fitting is computationally intensive and complicated given the *Kepler* FOV crowded stellar field and the significant PSF variations over that field (Bryson et al. 2010).

4. *KEPLER* ASTROMETRIC TESTS

These tests highlight several systematic errors and motivate our simple strategy for dealing with them. We employ GaussFit

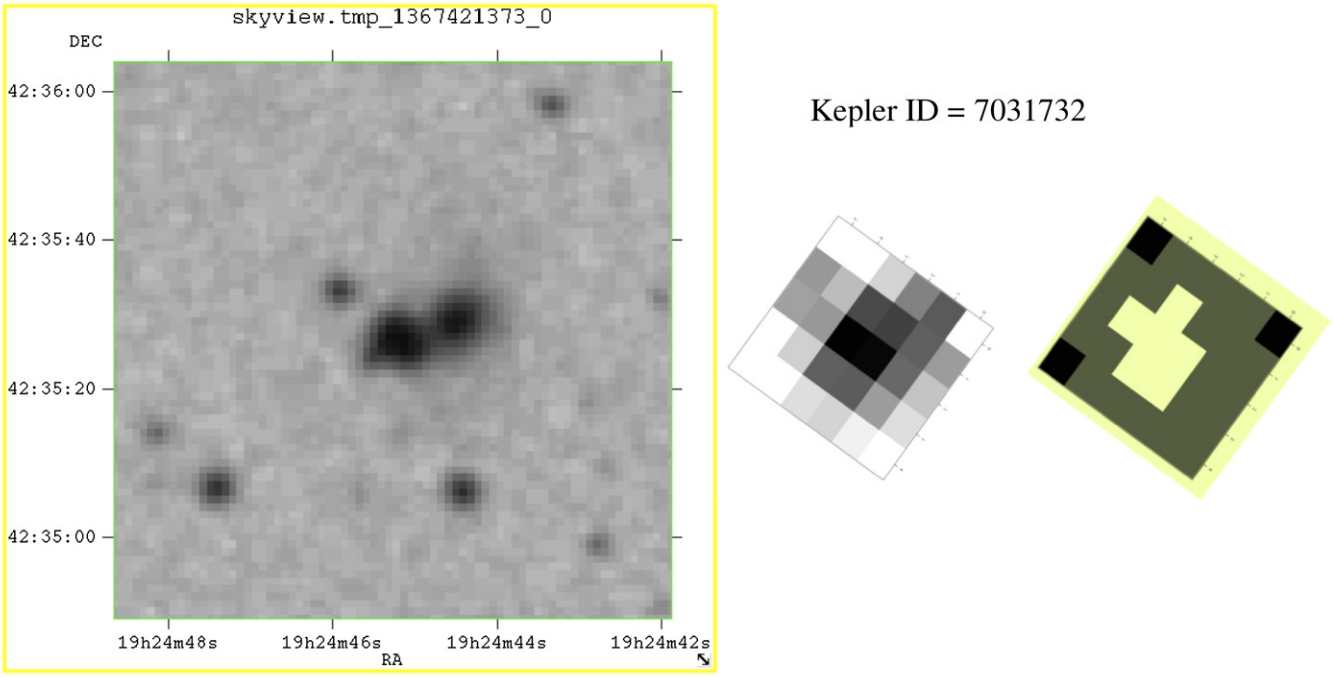

Figure 3. Left: KID 7031732 in a crowded field. Image from Digital Sky Survey via *Aladin*. Middle: postage stamp for KID 7031732. Right: optimum aperture for KID 7031732.

(A color version of this figure is available in the online journal.)

for all of our astrometric modeling (Jefferys et al. 1988) to minimize χ^2.

4.1. Single Channel, Single Season, Single Quarter

These tests use 95 stars located in Channel 21, Season 0, Quarter 10 that are identified as red giants in the *Kepler* Input Catalog (KIC). This initial filtering by star type potentially minimizes any effects of proper motion over the span of one or even two quarters. The NP generator, run on each star selected from test Channel 21, effectively reduces the number of discrete data sets per star from on the order of 4500 down to 9. We assign the 9 NPs for each of the 95 stars in the test to the 9 "plates." Each plate now contains 95 stars whose epochs are separated in time by approximately 9 days. Using the positions and positional errors generated by the NP code (now organized as 9 "plates" each containing 95 star positions and associated errors), we determine scale, rotation, and offset "plate constants" relative to an arbitrarily adopted constraint epoch (the so-called "master plate") for each observation set (the positions generated for each star within each "plate" at each of the nine NP epochs). The solved equations of condition are

$$\xi = Ax + By + C, \tag{3}$$

$$\eta = -Bx + Ay + F, \tag{4}$$

where x and y are the measured NP coordinates from the *Kepler* postage stamps. A and B are scale and rotation plate constants, C and F are offsets. For this test spanning only a single 90 day quarter, we ignore proper motions. When modeling these positions, in order to approach a near-unity χ^2/DOF (DOF = degrees of freedom), the input positional errors, standard deviations from the NP averaging process, had to be increased by a factor of four. The final catalog of (ξ, η) positions have average $\langle\sigma_\xi\rangle = 0.31$ millipixel and $\langle\sigma_\eta\rangle = 0.64$ millipixel (1.23 and 2.54 mas), which is seemingly quite encouraging if one's goal is precision astrometry with *Kepler*.

However, the results of this modeling, shown in Figure 4, exhibit large systematic effects that are well correlated with time. The constraint epoch for this reduction is JD−24400000 = 15785.2, that is, the middle epoch of the nine plotted. We tentatively blame the typically larger y residuals (y is larger than x within each epoch) in Figure 4 with charge-transfer smearing along the CCD column readout direction (Kozhurina-Platais et al. 2008; Quintana et al. 2010). Our ultimate goal is to tease out stellar positional behavior similarly correlated with time: proper motion. We find stars 9 (=KID 6363534) and 27 (=KID 6606001) to exhibit some of the largest and most strikingly systematic residual patterns. Figure 5 provides an explanation for the behavior of star 27 (a close companion that perturbed the simple first-moment centering algorithm), and presents a puzzle regarding star 9. This star has no bright companions, yet it is a poorly behaved component of our astrometric reference frame. We suspect that this is due to the CCD channel-to-channel cross-talk discussed in Caldwell et al. (2010b). Four CCDs share common readout electronics. A bright star on one CCD can affect the measured charge in another.

To determine whether or not there might be unmodeled—but possibly correctable—systematic effects at the 10 millipixel level, we plotted the reference frame x and y residuals against a number of parameters. These included the following: x, y position within the channel; radial distance from the channel center; reference star magnitude and color; and epoch of observation.

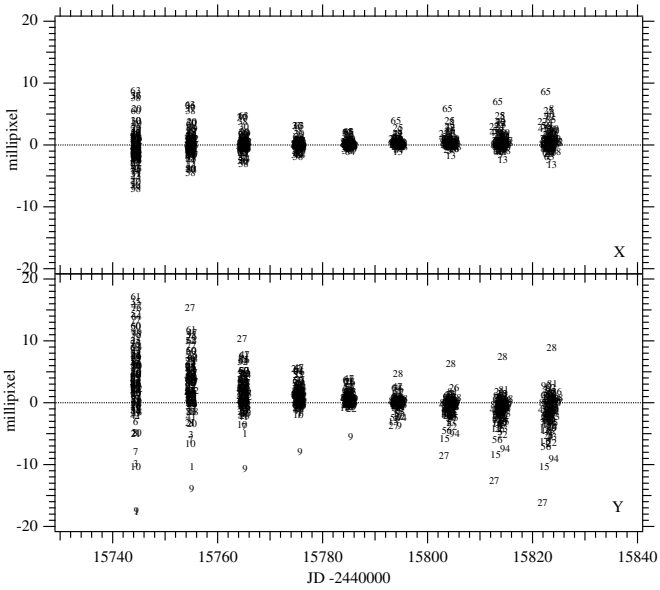

Figure 4. x and y residuals as a function of time for the Q10-only four parameter modeling from Section 4.1. The residual clumps from left to right are "plates" 1–9, the epochs of the averaged normal points. Stars are labeled with a running number from 1 to 97. The residuals exhibit significant time dependency. Regarding two of the stars with more extreme behavior, neither star 9 (=KID 6363534) nor star 27 (=KID 6606001) is a high-proper-motion object.

We saw no obvious trends, other than an expected increase in positional uncertainty with reference star magnitude. Models with separate x and y scales (six parameters; in Equation (2) above, where $-B$ and A are replaced by D and E) or color terms (eight parameters) provided no improvement in χ^2/DOF.

Given that the pipelined positions available in the _llc.fits files are also first-moment centroids calculated from the optimal apertures, we developed the capability to generate these independently as a further test of the *Kepler* astrometry. The code used to generate the positions whose residuals are plotted in Figure 4 can also produce first-moment centroid data using the entire postage stamp (e.g., all the flux values in the middle panel in Figure 3). By comparing the positions extracted from the entire postage stamp against the optimal subset of the postage stamp for Channel 21, the average absolute value residual is reduced by 30% when using the optimal apertures. However, tests carried out on Channel 41 (Season 0, Quarter 10) near the *Kepler* FOV center result in a much less significant improvement, only 12%. This can be explained by considering the degradation in the PSF from the center to the edge of the entire *Kepler* FOV (Bryson et al. 2010; Tenenbaum & Jenkins 2010).

4.2. Other Single-channel Tests

4.2.1. Same Stars—Multiple Seasons and Quarters

To test whether or not the peculiar fan pattern in the residuals against time seen in Figure 4 is channel-specific, we carried out similar tests for Channels 41–44, i.e., the four central CCDs in the *Kepler* focal plane. We sampled Quarters 3 through 14 using the same ∼75 stars in each channel. The results of this four parameter modeling are provided in Figure 6. Every quarter exhibits time-dependent residual behavior. The patterns often repeat within the same season. For example, in Season 1, the x residuals for star 5 (=KID 8949862) start out large and positive and move down to large and negative over ∼90 days.

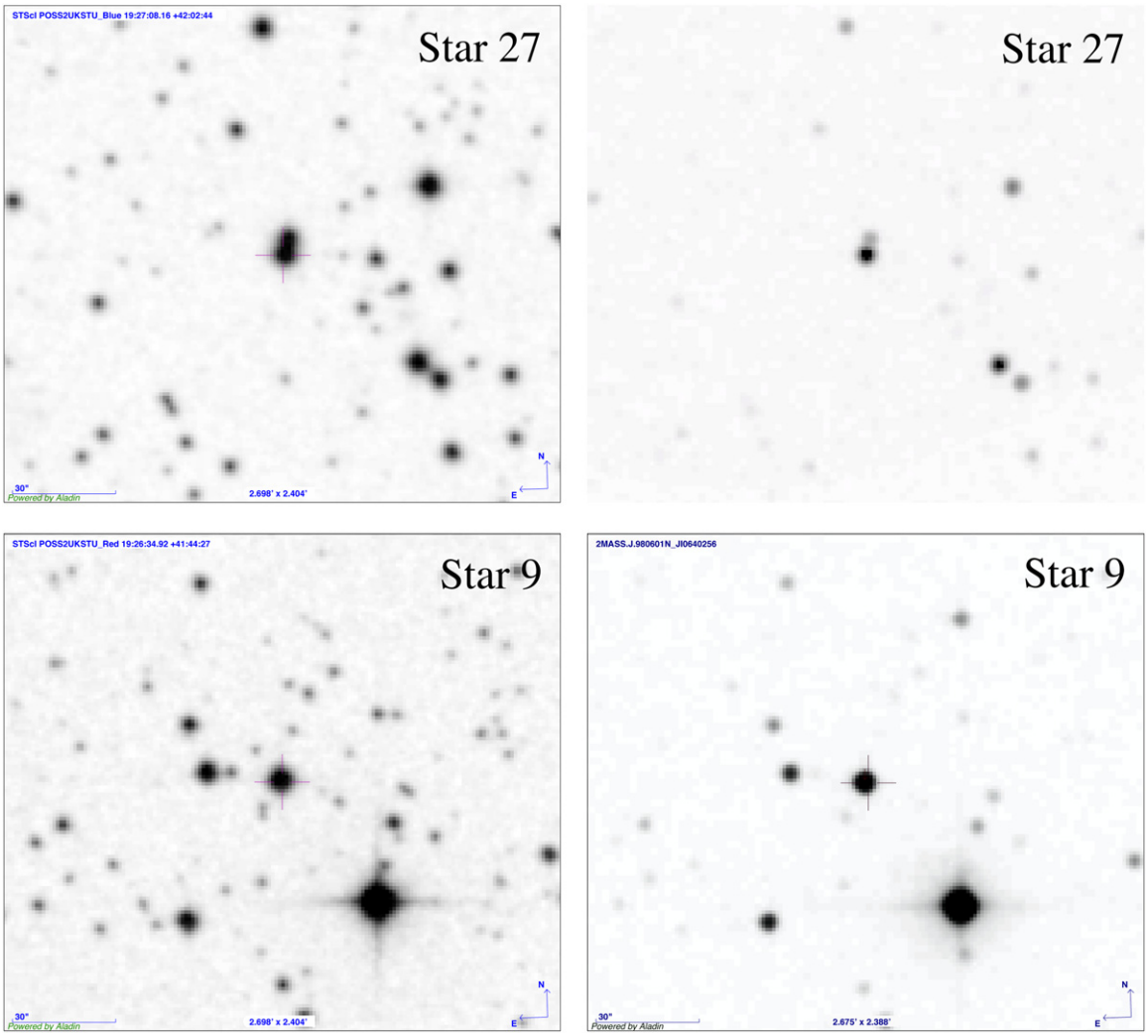

Figure 5. Top: star 27 (POSS-J on the left, 2MASS on the right) obviously with a close companion that confused the first-moment centering. Bottom: star 9, similarly illustrated. No companion to star 9 is detected. The positional shift is assumed to be instrumental.
(A color version of this figure is available in the online journal.)

However, star 5 is relatively well behaved for any other season. A comparison of Figure 6 with Figure 5 in Barclay (2011)[6] is convincing evidence that astrometry quality and primary mirror temperature changes are correlated. Stable temperatures at any level yield better astrometry (smaller residuals).

4.2.2. An External Check of Single-channel, Single-season Data

We carried out a four parameter modeling of 127 randomly chosen stars (a mix of dwarfs and giants according to the KIC) in Channel 26 from Season 3, Quarter 5 and found residual patterns similar to that for Season 3, Quarter 5, Channel 44 shown in Figure 6. We then extracted a subset of 10 stars, 5 with relatively well-behaved x residuals (stars 4–62) and 5 with x residuals that are not constant with time (stars 67–106 in Figure 7). We list these in Table 2.

To explore the hypothesis that astrophysical effects (i.e., companions undetectable at the resolution of the *Kepler* detectors) cause the observed residual behavior, these 10 stars were observed with the Keck NIRC2-AO system (Wizinowich et al. 2004; Johansson et al. 2008) on the nights of 2013 August 19–21 UT with the NIRC2 instrument on Keck II. The targets themselves were used as natural guide stars and observations were performed in the K' filter, or the Br-γ filter if the star was too bright for the broader K' filter. The native seeing on the three nights (before adaptive optics (AO)) was approximately 0.″6 at

Table 2
Companion Test Stars

#[a]	KID	KEPMAG	K	FluxFrac[b]
4	5698236	15.637	14.243	0.886
5	5698325	12.264	10.747	0.920
10	5698466	13.113	11.561	0.921
34	5783576	14.135	12.656	0.874
62	5784222	15.475	13.885	0.881
67	5784291	13.148	11.074	0.936
77	5869153	15.596	13.537	0.706
96	5869586	15.466	13.672	0.886
103	5869826	15.768	13.473	0.774
106	5870047	11.747	6.328	0.962

Notes.
[a] Numbering in Figure 7.
[b] Fraction of target flux in the *Kepler* project-defined optimum aperture.

[6] http://archive.stsci.edu/kepler/release_notes/release_notes12/DataRelease_12_2011113017.pdf

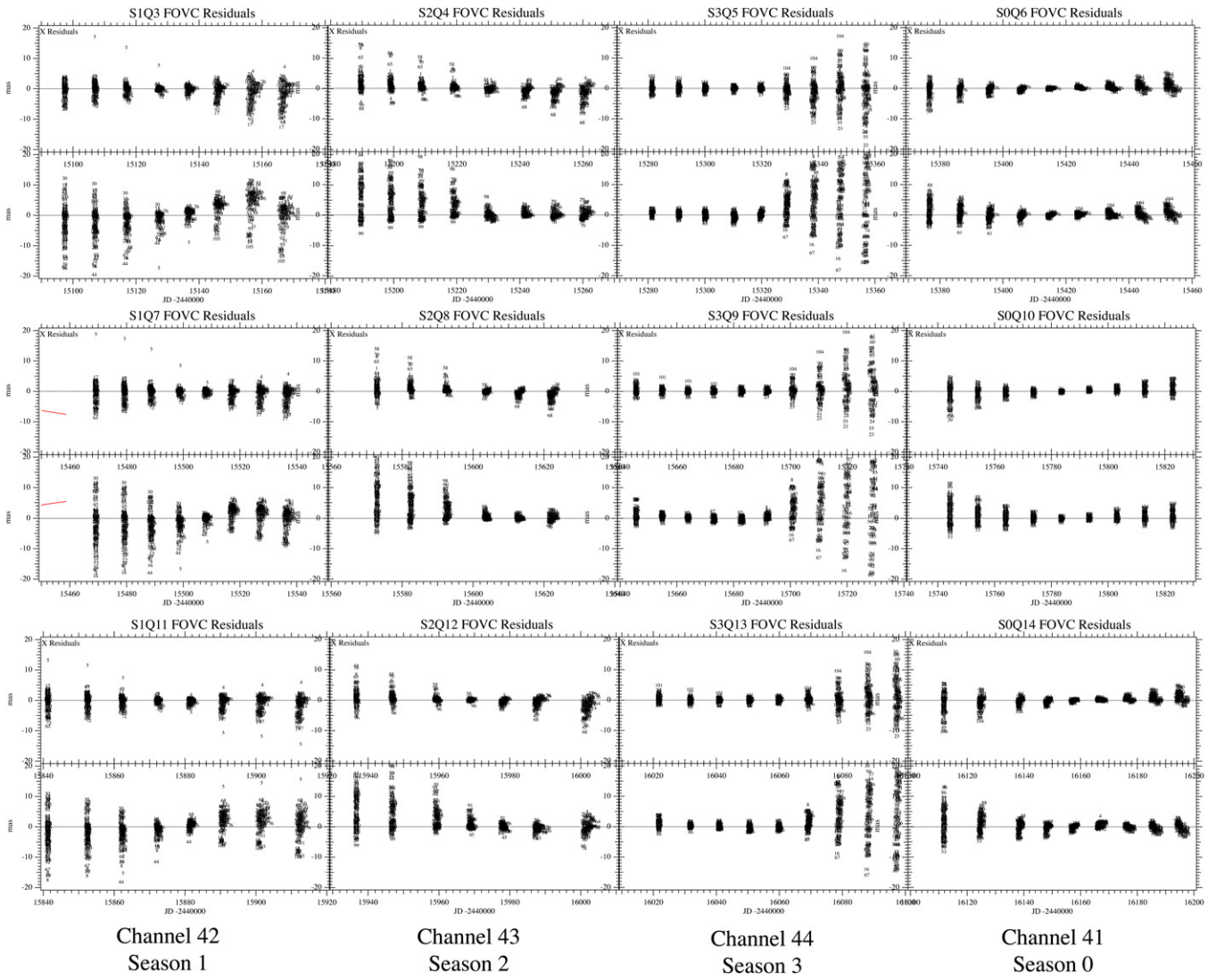

Figure 6. As in Figure 4, *x* and *y* residuals as a function of time for four parameter modeling of a sample of KIC-identified giants in Channels 41–44, but for 11 quarters. Top row, Quarters 3–6; middle row, Quarters 7–10; bottom row, Quarters 11–14. The top half of each box contains *x* residuals with *y* below. The *y*-axis range within each coordinate half-box is ±20 millipixels with an *x*-axis range between 80 and 90 days. The residuals exhibit time dependency within each quarter that correlates with focal plane temperature changes. Season 0 appears to have a larger fraction of stable astrometry.

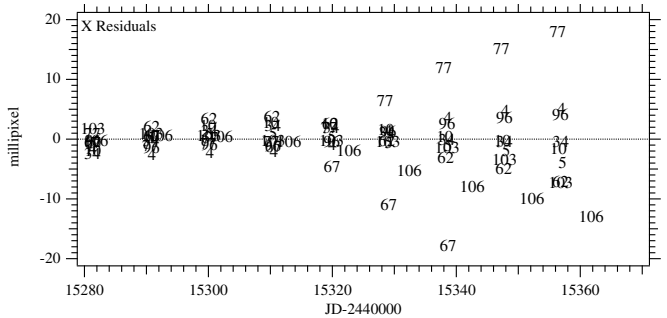

Figure 7. Selected *x* residuals as a function of time for four parameter modeling (Equations (3) and (4)) of 127 stars in Channel 26 from Season 3, Quarter 5. The star numbers are identified with *Kepler* IDs in Table 2. Note that stars [4,. . ., 62] are more astrometrically stable than stars [67,. . ., 106].

2 μm. The NIRC2 instrument was in the narrow field mode with a pixel scale of approximately 0.″009942 pixel^{-1} and a FOV of approximately 10.″1 on a side. Each data set was collected with a three point dither pattern, avoiding the lower left quadrant of the NIRC2 array, with five images per dither position, each shifted 1″ from the previous. Each frame was dark subtracted and flat fielded. The sky frames were constructed for each target from the target frames themselves by median filtering and coadding the 15 dithered frames. Individual exposure times varied depending on the brightness of the target but were typically 10–30 s per frame. Data reduction was performed using a custom set of IDL routines.

To estimate companion detection limits as a function of distance from the selected targets, we utilized PSF planting and cross correlation (Tanner et al. 2010). The science target was extracted from the image, sky subtracted, and normalized. Then it was added at random positions around the image such that an equal number of plant positions occur in each radius bin of 0.″1 around the science target. The flux within each planted PSF is scaled by a random value ranging from 10^{-3} to 10^{3} times the original number of counts in the star. The counts were determined through aperture photometry with a radius of 0.″2 and a sky annulus of 0.″2–0.″3. Once added to the image, the threshold for detection was established by cross-correlating the planted star with the normalized PSF. A scaled and random PSF plant was considered to be detected if the cross-correlation value

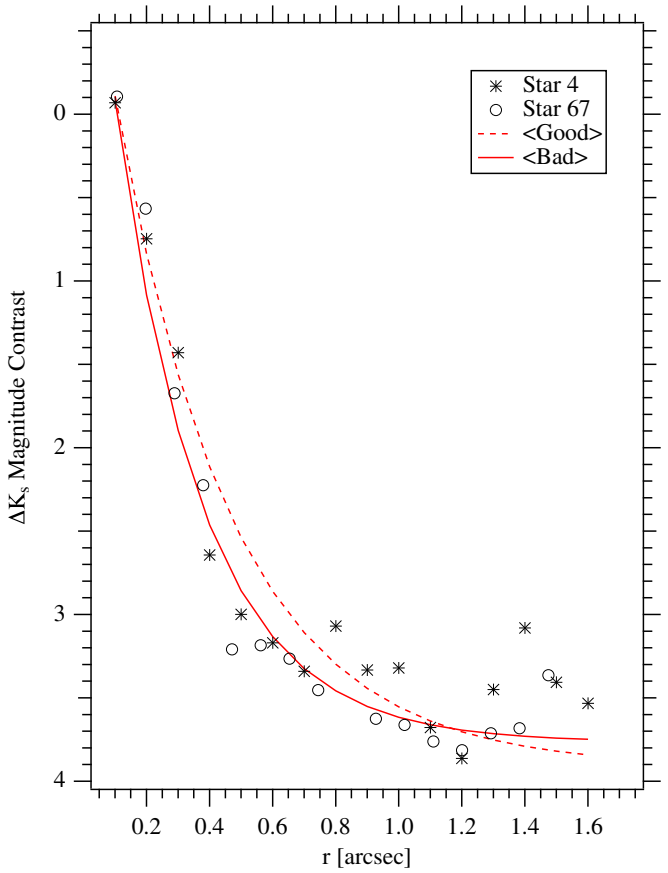

Figure 8. Normalized K-band contrast curves for stars 4 and 67, along with average contrast curves for stars 4 through 62 (Good) and 67 through 106 (Bad). Note that while star 4 is more astrometrically stable than star 67, they have virtually identical contrast curves.

(A color version of this figure is available in the online journal.)

was above 0.5—a value determined with a "by eye" assessment. The location and flux of those PSFs that were detected were recorded over 5000 PSF plants. In each radius bin, the PSF with the smallest flux was used in the resulting plot of detected minimum magnitude difference (ΔK_s) versus distance from the science target.

We found no companion candidates in these images within a radius of 1.″2. Figure 8 contains the contrast curves for star 4 (constant residuals) and star 67 (time-varying residuals), along with a fit to the normalized average contrast curves for stars 4–62 (⟨Good⟩) and 67–106 (⟨Bad⟩). To fit the average contrast curves, we employed an exponential function ($y = K0 + K1 * \exp(-(x - x0)/K2)$) with offset $x0$. The similarity of the average contrast curves removes small angular separation, fainter companions as the cause of the behavior displayed in Figure 7. Finally, the average Season 3 crowding, contamination, and flux fraction parameters (see Fraquelli & Thompson 2012 for parameter details) of the two groups differed little.

4.2.3. Lessons Learned

With as rich a data set as produced by *Kepler*, our approach is to exercise extensive editing to establish the best astrometric reference frame: a reference frame with χ^2/DOF $\sim$ 1 and Gaussian distribution of residuals. If we model only epochs 3–7 in Figure 4, as shown in Figure 9, we generate a final catalog of (ξ, η) positions with average $\langle\sigma_\xi\rangle = 0.22$ millipixel and $\langle\sigma_\eta\rangle = 0.46$ millipixel (0.87 and 1.83 mas). The residuals are Gaussian (Figure 10) and naturally larger than the average

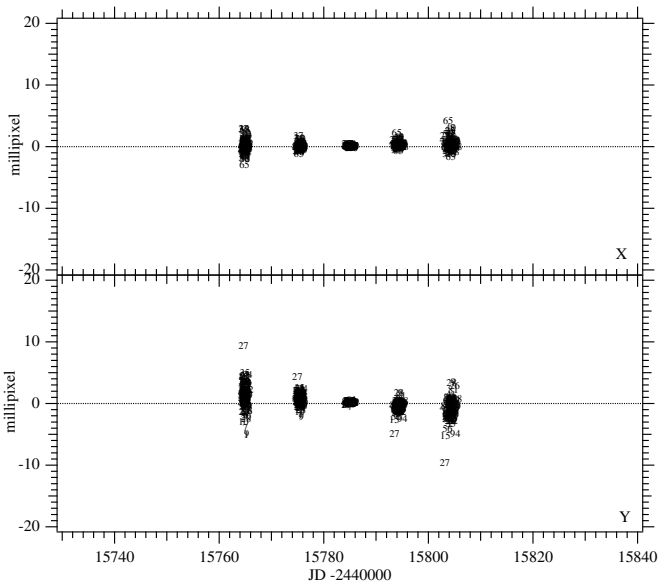

Figure 9. x and y residuals as a function of time for the Q10-only four parameter modeling from Section 4.1. The residual clumps from left to right are "plates" 3–7, first seen in Figure 4. Stars are labeled with a running number from 1 to 97. The residuals exhibit far less time dependency. Stars 9 and 27 continue to exhibit unmodeled behavior.

catalog errors because of the effective averaging to produce a catalog. Again, the significantly larger residuals along the y axis are likely due to CCD read-out issues (Kozhurina-Platais et al. 2008; Quintana et al. 2010).

4.3. Two Channels, Two Contiguous Seasons

Again restricting our test to include only stars identified as red giants to minimize proper-motion effects, we now run a plate overlap model for the same set of stars appearing on two different Channels (21, 37) for Quarters 10 and 11, respectively. Given that the average absolute value UCAC4 proper motion for this suite of test stars is 7.5 mas yr^{-1} (less than 2 millipixel yr^{-1}), the roughly 180 day span of these data should exhibit very little scatter due to unmodeled motions. A four parameter model (with the constraint plate chosen to be from Channel 21) yielded a final catalog with $\langle\sigma_\xi\rangle = 2.60$ millipixel and $\langle\sigma_\eta\rangle = 6.6$ millipixel (10.33 and 26.23 mas), which is significantly poorer astrometric performance than for a single channel and quarter (Section 4.1). A six parameter model with separate scales along x and y yielded only a 0.8% reduction in the large value of the reduced χ^2/DOF.

The *Kepler* telescope has a Schmidt–Cassegrain design. An effective astrometric model for such a telescope, used successfully in the past on Palomar Schmidt photographic plates, is introduced in Abbot et al. (1975) and used in, e.g., Benedict et al. (1978). That model,

$$\xi = Ax' + By' + Cx'y' + Dx'^2 + Ey'^2 + Fx'(x'^2 + y'^2) + G, \quad (5)$$

$$\eta = A'x' + B'y' + C'x'y' + D'x'^2 + E'y'^2 + F'y'(x'^2 + y'^2) + G', \quad (6)$$

when applied to the Channels 21 and 37 data, provided a 9.1% reduction in reduced χ^2/DOF, but a final catalog with errors almost exactly as found for the four and six parameter models. The run of residuals with time is shown in Figure 11. The residuals from this modeling are on average eight times larger

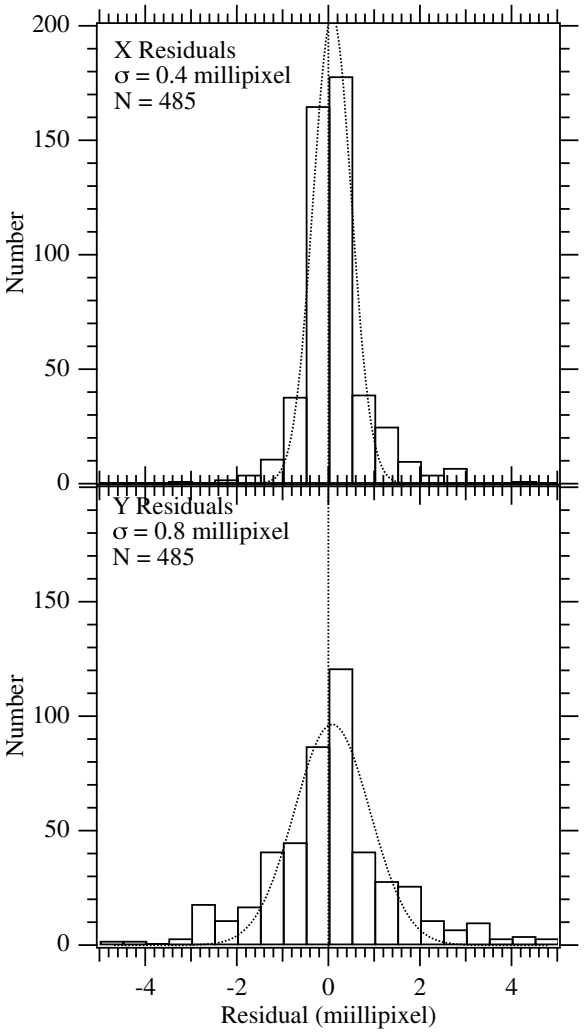

Figure 10. Histograms of x and y residuals for the Q10-only four parameter modeling of only plates 3–7 (Figure 9) from Section 4.1. The residuals are well characterized with Gaussians with 1σ dispersions as indicated.

than for Channel 21 alone. That the residuals remain large even with a Schmidt model demonstrates that the astrometric effects are not due to the Schmidt nature of the *Kepler* Telescope. The residuals as a function of position within the Channel 37 CCD show large variations on extremely small spatial scales (Figure 12). We have yet to identify the source of these high-frequency spatial defects, but cannot yet rule out the individual field flatteners atop each module containing four channels (Tenenbaum & Jenkins 2010). This inter-channel behavior effectively prohibits the measurement of precise parallaxes using only *Kepler* data.

5. ASTROMETRY OF A *KEPLER* TEST FIELD

Our ultimate goal is to produce an RPM diagram including KOIs, which would permit an estimate of their luminosity class. This may be feasible by restricting astrometry to a single channel and season. Essentially, we may be able to ignore the deficiencies demonstrated in Figures 11 and 12 because each star in any given season will be observed by the same pixels, and the starlight is passing through the exact same region of the field flattener. The 17 available quarters provide 3–4 same-season observation sets for any *Kepler* channel. Examination of Figure 6 supports our identification of Season 0 as one of the more stable. Tests similar to those carried out in Section 4.1

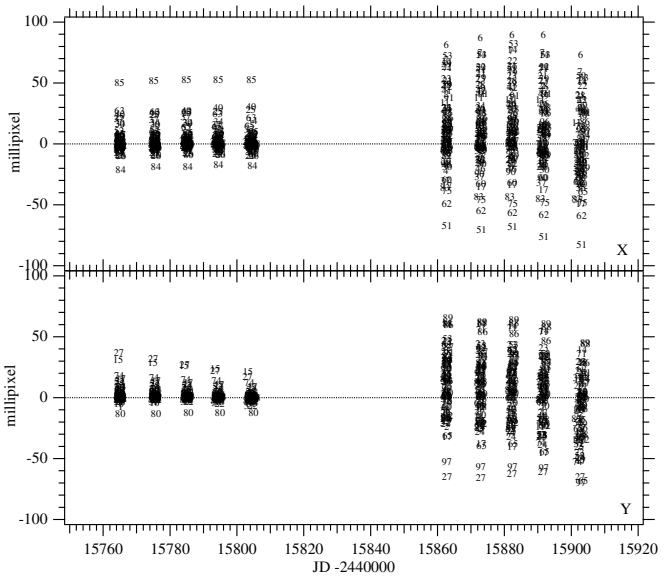

Figure 11. x and y residuals in millipixels as a function of time from the full Schmidt 14 parameter modeling from Section 4.3. The residual clumps on the left-hand side (Channel 21) from left to right are "plates" 3–7. Stars are labeled with a running number from 1 to 97. Note the scale change along the y-axis, a range five times larger than that in Figure 9. The residuals exhibit extreme time dependence. Star 27 continues to show unmodeled behavior in both channels. Virtually all stars in Channel 37 (right) exhibit unmodeled behavior.

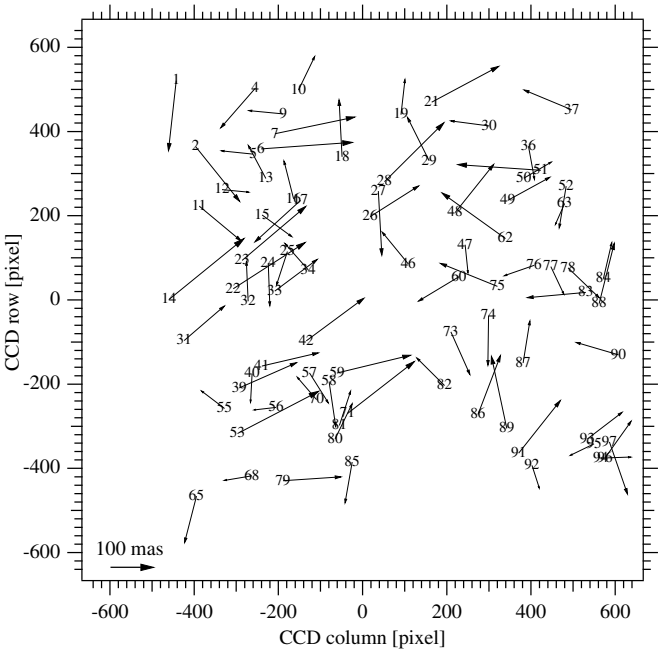

Figure 12. Average vector residuals in milliarcseconds (scale at lower left) as a function of position within Channel 37 from the full Schmidt 14 parameter modeling of Channel 21 and Channel 37 described in Section 4.3. All positions have been re-origined to the CCD center. Note the extreme variation in vector length and position angle over small spatial scales, for example, the grouping consisting of stars 22 through 34 (row $\sim$ 50, column ~ -200). Comparing Channel 21 with Channel 37 demonstrates serious astrometric systematics on very small spatial scales.

yielded very poor results for Quarter 2, and hence it is unused here.

5.1. Populating an RPM Diagram

To fully populate the H_K, $(J-K)_0$ plane of an RPM diagram, we extract Channel 21 long-cadence image data (*lpd-targ*) for

stars with 14 > KEPMAG > 11.6 (Quarters 6, 10, and 14, and all Season 0):

1. Approximately 100 stars classified as red giants;
2. Approximately 100 stars with $T_{\rm eff} > 6500$ K;
3. Approximately 100 stars with $6200 > T_{\rm eff} > 5100$ K;
4. Approximately 30 stars with $T_{\rm eff} < 5000$ K and Total_PM $\geqslant$ $0\farcs24{\rm yr}^{-1}$ with any KEPMAG value; and
5. All KOIs found in Channel 21, e.g., *Planetary_candidate* and *Exoplanet_host_star* condition flag objects. These also have unrestricted KEPMAG.

We extract positions and generate nine day average NPs using only the *Kepler* team defined optimal apertures for each star. When including these data in our modeling with the ground-based catalogs, we re-origin the *Kepler* x, y coordinate values to (0,0) at the center of Channel 21.

5.2. Reference Star Priors

To place our relative astrometry onto a right ascension (R.A.), declination (decl.) system, we extract J2000 positions and proper motions from the UCAC4 (Zacharias et al. 2013) and PPMXL (Roeser et al. 2010) catalogs. The catalog positions scale the *Kepler* astrometry and provide an approximately 12 yr baseline for proper-motion determination. Additionally, the catalog proper motions with associated errors are entered into the modeling as quasi-Bayesian priors. These values are not entered as hardwired quantities known to infinite precision. The χ^2 minimization is allowed to adjust the parameter values suggested by these data values within limits defined by the data input errors.

The input positional errors average 19 mas for the UCAC4 and 63 mas for the PPMXL. The average per-axis proper-motion errors are 2.6 mas yr^{-1} for UCAC4 and 3.9 mas yr^{-1} for PPMXL. A comparison of the two catalogs yields an average per-star absolute value proper-motion disagreement of 5.1 mas yr^{-1}, indicating that there is room for improvement. The R.A. and decl. positions from the two catalogs are used to calculate ξ, η standard coordinates transformed from radians to arcseconds (van de Kamp 1967) using the center of Channel 21 as the tangent point.

5.3. The Proper-motion Astrometric Model

Using the central five epochs of positions from Quarters 6, 10, and 14 from *Kepler* Channel 21 (the editing of each quarter can be illustrated by comparing Figure 4 to Figure 9), spanning 2.14 yr, with standard coordinates from PPMXL and UCAC4, and proper-motion priors from the latter two catalogs, we determine "plate constants" relative to the UCAC4 catalog (this catalog having smaller formal positional errors). The constraint epoch is thus 2000.0. Our reference frame after pruning out astrometrically misbehaving objects contains 226 stars. For this model, we include only those stars with a restricted magnitude range, 14 > KEPMAG > 11.6 (samples 1–3 discussed in Section 5.1 above). The average magnitude for this magnitude-selected reference frame is $\langle$KEPMAG$\rangle = 13.3$.

Again, we employ GaussFit (Jefferys et al. 1988) to minimize χ^2. The solved condition equations for the Channel 21 field are now

$$\xi = Ax' + By' + Cx'y' + Dx'^2 + Ey'^2 + Fx'(x'^2 + y'^2) + G - \mu'_x\Delta t, \quad (7)$$

$$\eta = A'x' + B'y' + C'x'y' + D'x'^2 + E'y'^2 + F'y'(x'^2 + y'^2) + G' - \mu'_y\Delta t, \quad (8)$$

where $x' = x - 500$ and $y' = y - 500$ are the re-origined measured coordinates from *Kepler* and the standard coordinates from UCAC4 and PPMXL; μ_x and μ_y are proper motions; and Δt is the epoch difference from the mean epoch.

Based on the resulting astrometric parameters, we form a plate scale of

$$S = (BA' - AB')^{1/2}, \quad (9)$$

and for the 15 epochs (five for each of the three quarters) of *Kepler* observations find $\langle S\rangle = 3\farcs97664 \pm 0\farcs000009$ pixel^{-1}, which is close to the nominal *Kepler* plate scale (van Cleve & Caldwell 2009) and an indication that the *Kepler* telescope plate scale as sampled in Channel 21 was quite constant. The scale factor of the PPMXL catalog relative to the UCAC4 catalog was 1.000012.

5.4. Assessing the Reference Frame

Using the UCAC4 catalog as the constraint plate to achieve a χ^2/DOF $\sim$ 1, the *Kepler* NP data errors (NP standard deviations) had to be increased by a factor of 16. Histograms of the *Kepler* NP residuals were characterized by $\sigma_x = 3.6$ mas, $\sigma_y = 6.4$ mas. The average absolute value residual for *Kepler* was 4.8 mas, 24.3 mas for UCAC4, and 61.6 mas for PPMXL. The resulting 226 star reference frame "catalog" in ξ and η standard coordinates was determined with average positional errors of $\langle\sigma_{\xi,\eta}\rangle = 8.6$ mas, a 55% improvement in relative position over the UCAC4 catalog. The average proper-motion error for the stars comprising the reference frame is 0.8 mas yr^{-1}.

Again, to determine whether or not there might be unmodeled—but possibly correctable—systematic effects, we plotted the reference frame x and y residuals against a number of parameters. These included the x, y position within the channel (Figure 13), the radial distance from the channel center, the reference star magnitude and color, and the epoch of observation. We saw no obvious trends other than an expected increase in positional uncertainty with reference star magnitude. Plots of x and y residual versus pixel phase also indicated no trends. We calculate the pixel phase, $\phi_x = x - {\rm int}(x + 0.5)$, where int returns the integer part of the (for example) x coordinate.

5.5. Applying the Reference Frame

To ensure that the typically fainter (and hence less valuable contributors to the astrometric reference frame) stars do not affect our astrometric modeling of the Channel 21 CCD, an identical model in Section 5.3 is re-run, adding NP positions for the K and M stars (sample 4) and KOIs (sample 5) from Section 5.1, holding the Equations (7) and (8) coefficients A–G' to the values determined in Section 5.3. Note that we do solve for the positions and proper motions. This yields final catalog positions and proper motions for 301 stars representing all the categories listed in Section 5.1. The inclusion of fainter stars results in a "catalog" with ξ and η standard coordinates average relative positional errors $\langle\sigma_{\xi,\eta}\rangle = 11.1$ mas, and an average proper-motion error for all stars of 1.0 mas yr^{-1}. The decrease in proper-motion precision relative to that found for the reference-frame-only stars is driven by the inclusion of the typically fainter K, M, and KOI stars with average $\langle$KEPMAG$\rangle = 15.1$. As shown in Section 5.7 below, the centroids of fainter stars

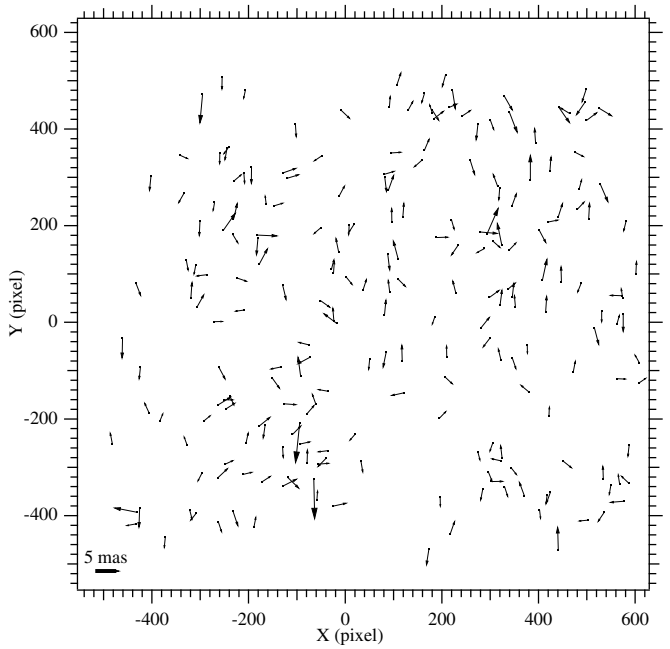

Figure 13. Average vector residuals in milliarcseconds as a function of position within Channel 21 from the full Schmidt 14 parameter modeling of three Season 0 observation sets described in Section 5.3. Other than a strong tendency for larger residuals in the y direction, the pattern is satisfactorily random.

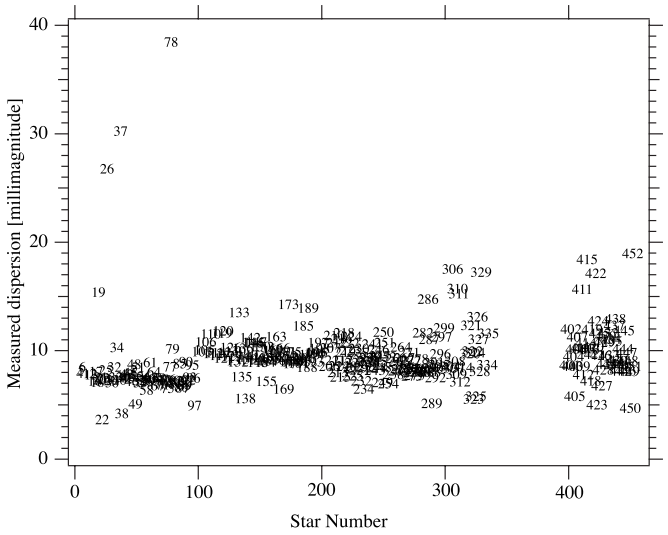

Figure 14. Measured photometric dispersion (m_f standard deviation) over 2.1 *y* with a nine day cadence for each star modeled in Section 5.3. Giants (1–100) exhibit the highest overall variability. Other groups are the hot star sample (101–199), mid-range $T_{\rm eff}$ (201–299), the K–M star sample (300–350), and the KOI sample (400–452). The trends to smaller photometric variation with number within each sample group (as defined in Section 5.1) may be a function of position within Channel 21. The lowest variations are closer $(x, y) = (0, 1000)$ while the highest are closer $(x, y) = (1000, 0)$.

have lower signal to noise and, if included, would degrade our astrometric reference frame.

We present final KOI proper motions and errors in Table 3. These are, in a sense, absolute proper motions because of the use of prior information. To reiterate, we treated the UCAC4 and PPMXL proper-motion priors as observations with corresponding errors. The Table 3 KOI proper-motion parameters (and those for the entire set of reference stars modeled above) were adjusted by various amounts depending on the data input errors to arrive at a final result that minimized χ^2.

5.6. Reference Star Photometric Stability

Our NP generation process (Section 3.2) also produces an average magnitude. In the case of nine day NPs, all of the measured flux values in each optimum aperture are averaged over the nine day interval and converted to a magnitude with an arbitrary zero point through $m_f = 25.768–2.5^* \log_{10}(\langle \text{flux} \rangle)$. Because we restricted this test to a single channel, no background correction is applied. The standard deviation for the 15 average m_f magnitudes is plotted against reference star ID number in Figure 14. Referencing Section 5.1, stars 1–99 are classified as red giants in the KIC (sample 1), stars 100–199 are hotter stars (sample 2), stars 201–299 are intermediate temperature stars (sample 3), stars 300–350 are selected to be more likely K and M dwarfs (sample 4), and stars 400–452 are the KOIs found in Channel 21 (sample 5). Note that all ID numbers are not present in the plot due to the editing process (Section 5.3) that produces the final astrometric reference frame.

The highest maximum variability with a nine day cadence is found in our sample of suspected giants, which was not an unexpected result (Bastien et al. 2013). The KOIs seem to have photometric variability characteristics most similar to the K, M group. We note trends toward smaller variation with increasing number within each group (as defined in Section 5.1). This may be a function of photometric noise characteristics having positional dependence within Channel 21. The selection process populating each group and allocating a running number within each group always assigned the lowest numbers closer to (x, y)=(0, 1000) and the highest closer to $(x, y) = (1000,0)$.

5.7. Astrometry as a Diagnostic

Figure 15 contains an average absolute value *Kepler x* residual for each reference star and KOI (numbering from Table 3) as a function of m_f. The residuals are calculated from the Section 5.3 modeling results. We choose the *x* residual as a potential diagnostic given that the *y* residuals are generally systematically larger (see Figures 10 and 13). The trend line is a quadratic fit to the *x* residuals for the reference stars only (samples 1–3 in Section 5.1). The planet-hosting KOIs over-plotted with large font show no extreme astrometric behavior, all lying within $\pm 3\sigma$ of the relation. However, several KOI hosting unconfirmed planetary companions exhibit astrometric peculiarities. Both KOI 426 and 452 were inspected in 2MASS and Palomar Sky Survey images and showed no nearby stellar companions or image structure indicative of close stellar companions. In addition, KOI 452 is the most photometrically variable (Figure 14) host candidate star. Unfortunately, given the random eruption of astrometric peculiarity (see Figure 5), astrometry alone cannot serve as a reliable indicator of astrophysically interesting behavior.

5.8. RPM Diagrams: Pre- and Post-Kepler

We now have the proper motions required to generate $H_K(0)$ values for an RPM (Section 2). *K*-band magnitudes, $J - K$ colors, and interstellar extinction values, A_V, $E(B - V)$, were extracted from the online *Kepler* target database at MAST. We assumed (Schlegel et al. 1998) extinction-corrected by $K(0) = K - A_K$ and $(J - K)_0 = (J - K) - E(J - K)$, with $A_K = A_V/9$ and $E(J - K) = 0.53^* E(B - V)$. The left-hand RPM in Figure 16 shows $H_K(0)$ and $(J - K)_0$ for all stars except the KOIs and exhibits a distribution of points that appears to have a

Table 3
Channel 21 KOI Proper Motions (μ)

ID	KID	KOI	m_f	μ_{RA}[a]	μ_{DEC}[b]	μ_T
401	6362874	1128	13.51	−0.0063 ± 0.0008	−0.0307 ± 0.0008	0.0314 ± 0.0011
402	6364215	2404	15.66	0.0005 0.0015	−0.0056 0.0019	0.0056 0.0024
403	6364582	3456	12.99	0.0022 0.0011	0.0029 0.0005	0.0036 0.0012
404	6441738	1246	14.90	−0.0038 0.0013	0.0158 0.0012	0.0163 0.0017
405	6442340	664	13.48	0.0090 0.0009	−0.0103 0.0011	0.0137 0.0015
406	6442377	176	13.43	0.0079 0.0009	0.0096 0.0012	0.0124 0.0015
407	6520519	4749	15.61	0.0026 0.0017	−0.0061 0.0019	0.0067 0.0025
408	6520753	4504	11.20	0.0046 0.0087	−0.0535 0.0061	0.0537 0.0106
409	6521045	41	15.20	0.0205 0.0003	−0.0275 0.0006	0.0343 0.0007
410	6522242	855	15.98	0.0025 0.0037	0.0128 0.0029	0.0130 0.0047
411	6523058	4549	13.16	0.0041 0.0019	0.0024 0.0017	0.0048 0.0025
412	6523351	3117	11.38	0.0052 0.0006	−0.0021 0.0006	0.0056 0.0009
413	6603043	368	15.90	−0.0029 0.0005	−0.0018 0.0004	0.0034 0.0006
414	6604328	1736	13.80	0.0033 0.0026	0.0026 0.0021	0.0042 0.0034
415	6605493	2559	15.55	−0.0052 0.0011	−0.0076 0.0012	0.0092 0.0016
416	6606438	2860	13.42	0.0044 0.0025	0.0051 0.0020	0.0068 0.0032
419	6607447	1242	13.75	0.0087 0.0009	0.0002 0.0014	0.0087 0.0017
420	6607644	4159	14.50	−0.0070 0.0017	0.0395 0.0018	0.0402 0.0025
421	6690082	1240	14.47	−0.0027 0.0010	−0.0130 0.0012	0.0133 0.0015
422	6690171	3320	15.95	0.0060 0.0021	−0.0027 0.0015	0.0066 0.0026
423	6690836	2699	15.23	−0.0081 0.0031	−0.0026 0.0019	0.0085 0.0036
424	6691169	4890	15.77	−0.0006 0.0016	−0.0105 0.0021	0.0106 0.0026
425	6693640	1245	14.20	0.0098 0.0012	0.0059 0.0013	0.0115 0.0018
426	6773862	1868	15.22	−0.0089 0.0024	−0.0014 0.0020	0.0091 0.0031
427	6774537	2146	15.33	−0.0023 0.0014	0.0026 0.0013	0.0035 0.0019
428	6774880	2062	15.00	0.0024 0.0019	−0.0019 0.0016	0.0031 0.0025
429	6776401	1847	14.81	−0.0031 0.0014	−0.0295 0.0015	0.0297 0.0020
430	6779260	2678	11.80	0.0000 0.0006	0.0063 0.0004	0.0063 0.0007
431	6779726	3375	15.70	0.0011 0.0031	−0.0084 0.0024	0.0085 0.0040
432	6862721	1982	15.77	0.0026 0.0017	0.0051 0.0022	0.0057 0.0027
433	6863998	867	15.22	0.0076 0.0014	0.0054 0.0012	0.0093 0.0019
434	6945786	3136	15.74	0.0088 0.0018	0.0010 0.0019	0.0089 0.0026
435	6946199	1359	15.23	0.0291 0.0032	−0.0082 0.0023	0.0303 0.0040
436	6947164	3531	14.62	−0.0002 0.0009	0.0010 0.0013	0.0011 0.0016
437	6947668	3455	15.80	−0.0027 0.0015	−0.0046 0.0017	0.0054 0.0023
438	6948054	869	15.60	0.0112 0.0023	0.0097 0.0020	0.0148 0.0031
439	6948480	2975	15.31	−0.0030 0.0013	−0.0004 0.0013	0.0030 0.0018
440	6949061	1960	14.13	0.0050 0.0012	−0.0022 0.0010	0.0055 0.0015
441	6949607	870	15.04	−0.0003 0.0017	0.0216 0.0019	0.0216 0.0026
442	6949898	3031	15.27	−0.0020 0.0021	−0.0021 0.0015	0.0029 0.0026
443	7031517	871	15.22	0.0066 0.0021	−0.0072 0.0014	0.0097 0.0025
444	7032421	1747	14.79	0.0088 0.0020	0.0160 0.0026	0.0182 0.0033
445	7033233	2339	15.13	0.0102 0.0016	0.0072 0.0017	0.0125 0.0023
446	7033671	670	13.77	0.0034 0.0008	−0.0076 0.0007	0.0083 0.0011
447	7115291	3357	15.19	0.0030 0.0018	−0.0014 0.0013	0.0034 0.0023
448	7115785	672	14.00	−0.0078 0.0011	−0.0117 0.0012	0.0141 0.0016
449	7118364	873	15.02	0.0072 0.0018	−0.0040 0.0015	0.0083 0.0023
450	7199060	4152	12.97	−0.0047 0.0010	−0.0028 0.0005	0.0054 0.0011
451	7199397	75	10.78	−0.0019 0.0007	0.0265 0.0006	0.0266 0.0009
452	7199906	1739	15.13	0.0029 0.0014	0.0041 0.0018	0.0050 0.0022

Notes.
[a] Proper motions in arcseconds per year.
[b] Corrected for cosδ declination.

main sequence and an ascending sub-giant branch. The average $H_K(0)$ error is 0.43 mag, but is dependent on the value of μ_{vec} with an increased error toward bright values of $H_K(0)$.

The scatter in the left of Figure 16 can be due to several causes. These causes include proper-motion accuracy, random motions of stars, and systematic motions of stars. The $H_K(0)$ average error bar in the figure indicates a ±0.4 mag of scatter due to measurement errors. The amount due to random stellar motions is unknown. Any particular star could have a large radial component to its random motion and be erroneously placed among the giant stars with typically lower than average proper motions. Those two effects increase the random scatter in an RPM. That systematic motions can corrupt an RPM is illustrated in Benedict et al.'s (2011) Figure 3. There, the RR Lyr variables all lie below and blueward of the broad main sequence. These Pop II giant stars have anomalously large proper motions, causing their erroneous placement in the RPM.

Comparing the *HST*-derived RPM (Figure 1, right) with the left-hand RPM in Figure 16 yields a systematic difference. What we identify as the locus of main-sequence stars from

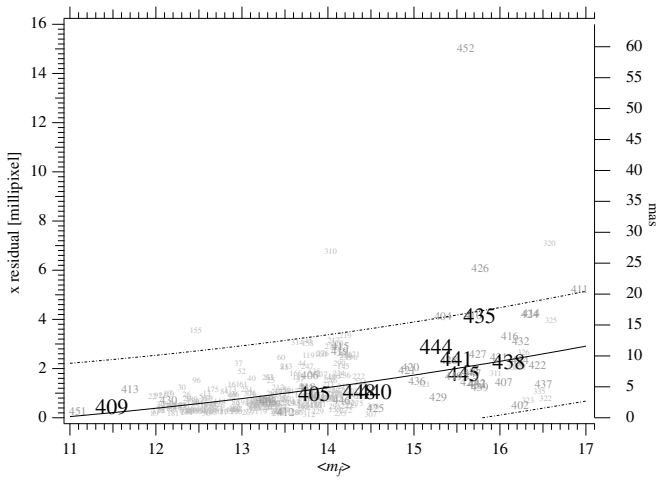

Figure 15. Average x residual from the Section 5.5 modeling plotted against average m_f, scaled in millipixel on the left and mas on the right. The solid curve is a quadratic fit to average reference star residuals resulting from the modeling in Section 5.3. Also plotted are the upper and lower bounds within which 99% of the Section 5.3 reference stars are expected to fall. These stars are plotted with the smallest ID numbers. The KOI are plotted with larger symbols. The nine confirmed planetary system host stars are plotted with large bold symbols. All KOI ID numbers are from Table 4. Clearly, KOI 426 and 452 are astrometrically peculiar, and the nine planetary system host stars behave as expected.

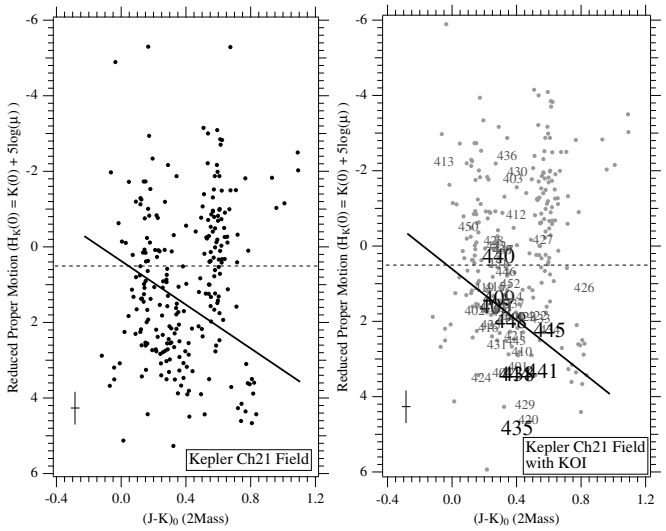

Figure 16. Left: RPM from the results of modeling *Kepler*, UCAC4, and PPMXL data. The average $H_K(0)$ and $(J-K)_0$ $\pm 1\sigma$ errors are indicated in the lower left. That error is reduced by a factor of three compared to an RPM derived by averaging proper motions from UCAC4 and PPMXL. The heavy, tilted line is the location of the main sequence in the Figure 1 RPM derived from all-sky *HST* proper motions. Note the vertical offset in $H_K(0)$ discussed in the text. Right: RPM with a $\Delta H_K(0) = -1.0$ correction, containing the KOI, also shifted. Plotted numbers are from Table 4. The horizontal dotted line represents a rough demarcation between giant and dwarf stars.

the right of Figure 1 appears to be substantially offset toward more negative $H_K(0)$ values by $\Delta H_K(0) = -1.0$. As a check, we produced an RPM by averaging the measured proper motions from the UCAC4 and PPMXL catalogs and obtain the same offset. Averaging the proper motions from the two catalogs, the typical $H_K(0)$ error is 1.58 mag, which is a factor of three larger than when we include *Kepler* astrometry. There is also a far greater increase in error for brighter values of $H_K(0)$.

To bring the main-sequence stars into coincidence with the *HST* main sequence would require decreasing the average $\mu_{\rm vec}$ proper motions of the final Table 3 proper motions by $\sim$10 mas yr^{-1}. This proper-motion offset is likely not from systematic effects on the proper motion due to the space velocity of the Sun. The *Kepler* field is very near the solar apex at R.A. $\simeq$ 287°, decl. $\simeq$ +37° (Vityazev & Tsvetkov 2013). With most of the vector of solar motion in the radial direction, stars near the solar apex will exhibit very little systematic proper motion due to solar motion. From Vityazev & Tsvetkov (2013), the average transverse velocity of stars in the solar neighborhood toward the Galactic center is $\bar{U} = 9$ km s^{-1}and the average transverse velocity perpendicular to the Galactic plane is $\bar{W} = 6$ km s^{-1} for a systematic total velocity of $V_t = 10.8$ km s^{-1}. Our sample of F–G dwarfs has $\langle K \rangle = 11.85$ mag with $\langle M_K \rangle \simeq 3$ (Cox 2000), and hence an average distance of 500 pc. The expected proper motion can be estimated from

$$\mu_{\rm vec} = \pi V_t / 4.74. \quad (10)$$

This yields $\mu_{\rm vec} = 4.6$ mas yr^{-1}, which could explain some but not all of the positive $H_K(0)$ offset in Figure 16.

However, as mentioned above in Section 2, a systematic effect of Galactic rotation on stellar velocities does exist. Our *HST*-derived RPM main sequence is composed of stars belonging to the Hyades and Pleiades star clusters. They have a Galactic longitude of $\ell \sim 175°$. The *Kepler* field has $\ell \sim 74°$. The velocity difference due to Galactic rotation is $\sim$30 km s^{-1}, translating to a proper-motion difference, $\Delta\mu_{\rm vec} =$ 12.7 mas yr^{-1}, close to the correction needed above.

We seek luminosity class differentiation, which is a relative determination within an RPM. We ascribe the need for a correction to bring the Channel 21 RPM into closer agreement with the right side of Figure 1 to a mix of the random and systematic proper motions just identified. We add the $\Delta H_K(0) = -1.0$ and replot this time including the KOI, similarly corrected for offset (right-hand side of Figure 16). The identification numbers in this plot, KIC numbers, and KOI numbers are collected in Table 4.

6. ESTIMATED ABSOLUTE MAGNITUDES FOR CHANNEL 21 KOI

Table 4 contains the $H_K(0)$ values (corrected by $\Delta H_K(0) = -1.0$) derived from the Table 3 KOI proper motions and $K(0)$ magnitudes. The listed K-band absolute magnitudes, $M_K(0)$, are obtained using the Figure 2 calibration: $M_K(0) = 1.51 \pm 0.12 + (0.90 \pm 0.02) \times H_K(0)$. An $M_K(0)$, $(J-K)_0$ H-R diagram is shown in Figure 17. An H-R diagram constructed using $H_K(0)$ from the UCAC4 and PPMXL average proper motions has a distribution similar to Figure 17, but with significantly increased scatter. Nine stars in Channel 21 (Season 0) host confirmed planetary systems. Our number 409 is Kepler-100, hosting three confirmed planets (Marcy et al. 2014), and our number 441 is Kepler-28, hosting two confirmed planets (Steffen et al. 2012). Recently, Rowe et al. (2014) have statistically confirmed a number of multi-planet systems. All exoplanet host stars and associated companions found in the Channel 21 field are listed in Table 5. Most of their positions in the Figure 17 H-R diagram lie on or close to a solar-metallicity 10 Gyr old main sequence (Dartmouth Stellar Evolution model; Dotter et al. 2008). Our number 435 (KOI-1359) has a photometrically determined (and hence low-precision) lowest metallicity, presented in Table 5, that is consistent with sub-dwarf location on an H-R diagram, as indicated in Figure 17. The other eight confirmed planetary

Table 4
Channel 21 KOI Absolute Magnitude

ID	KID	KOI	K_0	$(J-K)_0$	$H_K(0)$[a]	M_K[b]	Status[c]
401	6362874	1128	11.75	0.41	3.23 ± 0.08	4.4 ± 0.1	PC
402	6364215	2404	14.02	0.14	1.73 0.96	3.1 0.4	PC
403	6364582	3456	11.38	0.38	−1.76 0.71	−0.1 0.9	PC
404	6441738	1246	13.34	0.31	3.39 0.23	4.6 0.1	PC
405	6442340	664	11.96	0.27	1.65 0.23	3.0 0.1	Kepler-206b, c, d
406	6442377	176	12.18	0.24	1.65 0.26	3.0 0.1	PC
407	6520519	4749	13.77	0.39	1.90 0.81	3.2 0.3	PC
408	6520753	4504	13.94	0.43	6.59 0.43	7.4 0.1	PC
409	6521045	41	9.76	0.29	1.43 0.05	2.8 0.1	Kepler-100b, c, d
410	6522242	855	13.27	0.43	2.83 0.78	4.1 0.2	PC
411	6523058	4549	14.24	0.32	1.64 1.14	3.0 0.4	PC
412	6523351	3117	11.47	0.40	−0.80 0.34	0.8 1.7	PC
413	6603043	368	11.03	−0.05	−2.22 0.39	−0.5 0.3	PC
414	6604328	1736	14.24	0.38	1.37 1.73	2.7 0.7	PC
415	6605493	2559	12.30	0.27	1.12 0.38	2.5 0.2	PC
416	6606438	2860	14.04	0.23	2.19 1.03	3.5 0.3	PC
419	6607447	1242	12.43	0.20	1.14 0.42	2.5 0.2	PC
420	6607644	4159	12.60	0.47	4.62 0.14	5.7 0.1	PC
421	6690082	1240	12.81	0.39	2.41 0.26	3.7 0.1	PC
422	6690171	3320	13.79	0.53	1.88 0.85	3.2 0.3	EB; PC
423	6690836	2699	13.27	0.46	1.91 0.92	3.2 0.3	PC
424	6691169	4890	14.41	0.18	3.53 0.54	4.7 0.1	PC
425	6693640	1245	12.79	0.24	2.12 0.33	3.4 0.1	PC
426	6773862	1868	12.27	0.82	1.12 0.70	2.5 0.4	PC
427	6774537	2146	13.13	0.56	−0.15 1.16	1.4 1.3	PC
428	6774880	2062	13.45	0.26	−0.12 1.75	1.4 2.0	PC
429	6776401	1847	12.88	0.45	4.23 0.15	5.3 0.1	PC
430	6779260	2678	10.07	0.41	−1.96 0.23	−0.3 0.3	PC
431	6779726	3375	14.00	0.28	2.65 1.01	3.9 0.3	PC
432	6862721	1982	13.97	0.31	1.76 1.03	3.1 0.4	PC
433	6863998	867	13.11	0.55	1.94 0.44	3.3 0.2	PC
434	6945786	3136	13.52	0.61	2.24 0.63	3.5 0.2	PC
435	6946199	1359	13.48	0.40	4.88 0.28	5.9 0.1	R14
436	6947164	3531	13.06	0.34	−2.39 2.66	−0.6 1.8	EB; PC
437	6947668	3455	13.93	0.39	1.56 0.92	2.9 0.4	PC
438	6948054	869	13.59	0.41	3.45 0.45	4.6 0.1	Kepler-245b, c, d
439	6948480	2975	13.69	0.31	0.12 1.28	1.6 1.2	PC
440	6949061	1960	12.64	0.29	0.30 0.62	1.8 0.5	Kepler-343b, c
441	6949607	870	12.68	0.56	3.35 0.26	4.5 0.1	Kepler-28b, c
442	6949898	3031	13.61	0.28	0.02 1.83	1.5 2.1	PC
443	7031517	871	13.60	0.40	2.53 0.56	3.8 0.2	PC
444	7032421	1747	13.10	0.39	3.43 0.39	4.6 0.1	R14
445	7033233	2339	12.78	0.61	2.27 0.40	3.6 0.1	R14
446	7033671	670	12.15	0.33	0.72 0.28	2.2 0.2	PC
447	7115291	3357	13.49	0.32	0.11 1.45	1.6 1.3	EB; PC
448	7115785	672	12.32	0.37	2.04 0.25	3.3 0.1	Kepler-209b, c
449	7118364	873	13.34	0.37	1.91 0.62	3.2 0.2	PC
450	7199060	4152	11.84	0.10	−0.49 0.43	1.1 0.8	PC
451	7199397	75	9.37	0.29	0.50 0.08	2.0 0.1	PC
452	7199906	1739	13.43	0.36	1.01 0.93	2.4 0.5	PC

Notes.
[a] $H_K(0) = K(0) + 5\log(\mu_T)$ with $\Delta H_K(0) = -1.0$ correction.
[b] $M_K(0) = 1.51 \pm 0.12 + (0.90 \pm 0.02) \times H_K(0)$ from the Figure 2 calibration.
[c] PC = Planetary candidate, EB = eclipsing binary, FP = false positive, Kepler = designated exoplanets have been confirmed, R14 = statistical multi-exoplanet confirmation (Rowe et al. 2014).

system hosts have locations in the H-R diagram consistent with a main-sequence dwarf classification.

Inspection of Figure 17 suggests that a significant number of our astrometric reference stars (and some of the KOI) appear to be sub-giants. As with any apparent-magnitude-limited survey, the stars observed with *Kepler* will have a Malmquist-like bias, i.e., the survey will be biased toward the inclusion of the most luminous objects in the field as a result of the greater volume being surveyed for these intrinsically brighter objects (Malmquist & Hufnagel 1933). Therefore, within the *Kepler* field, there is a significant bias toward observing stars that are more massive and/or more evolved.

The *Kepler* target selection attempted to mitigate this bias by selecting stars identified as main-sequence solar-type dwarfs

Table 5
Channel 21, Season 0 Planetary Systems

ID	KID	KOI	Planet[a]	P(days)	Reference[b]	$T_{\rm eff}$	$R_\odot$	log g	[Fe/H]	$(J-K)_0$	$M_K(0)$
405	6442340	664.01	206c	13.1375	R14	5764	1.19	4.24	−0.15	0.27	3.0 ± 0.1
		664.02	206b	7.7820							
		664.03	206d	23.4428							
409	6521045	41.01	100b	12.816	Mar14	5825	1.49	4.13	+0.02	0.29	2.8 0.1
		41.02	100c	6.887							
		41.03	100d	35.333							
435	6946199	1359.01		37.101	R14	5985	0.85	4.53	−0.51	0.4	5.9 0.1
		1359.02		104.8202							
438	6948054	869.01	245b	7.4902	R14	5100	0.80	4.56	−0.03	0.41	4.6 0.1
		869.02	245d	36.2771							
		869.03	245c	17.4608							
440	6949061	1960.01	343b	8.9686	R14	5807	1.43	4.18	−0.14	0.29	1.8 0.5
		1960.02	343c	23.2218							
441	6949607	870.01	28b	5.9123	R14	4633	0.67	4.65	+0.34	0.56	4.5 0.1
		870.02	28c	8.9858	Ste12						
444	7032421	1747.01		20.5585	R14	5658	0.89	4.54	+0.07	0.39	4.6 0.1
		1747.02		0.5673							
445	7033233	2339.01		2.0323	R14	4666	0.68	4.64	+0.38	0.61	3.5 0.1
		2339.02		65.1900							
448	7115785	672.01	209b	41.7499	R14	5513	0.94	4.47	+0.01	0.37	3.4 0.1

Notes.
[a] Assigned number in the *Kepler* confirmed planet sequence, e.g., Kepler-206c.
[b] Mar14 = Marcy et al. (2014), Ste12 = Steffen et al. (2012), R14 = Rowe et al. (2014).

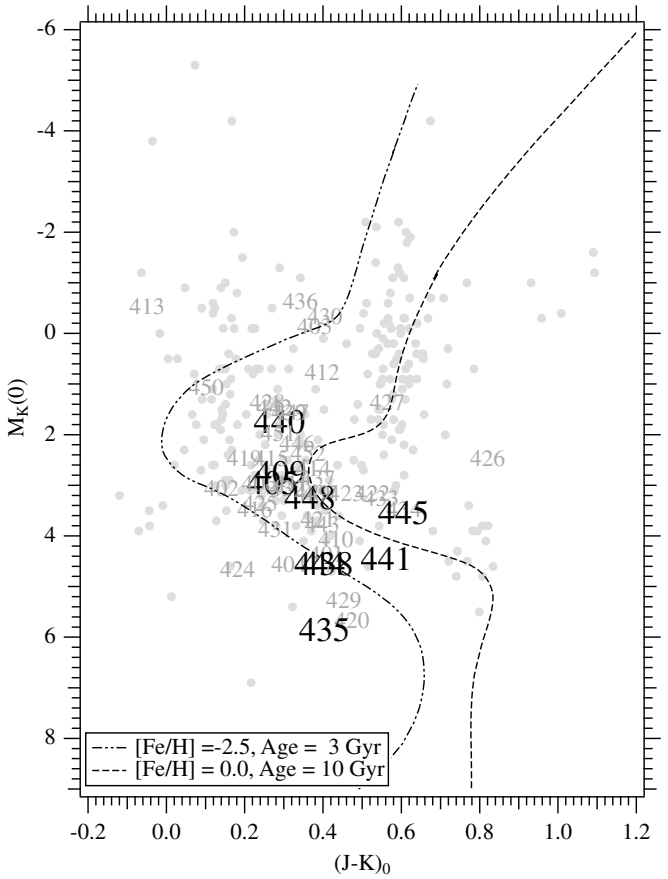

Figure 17. H-R diagram for the Section 5.5 reference stars and the Table 4 KOIs. $M_K(0)$ are calculated using the Figure 2 linear mapping between $M_K(0)$ and $H_K(0)$ after applying the Section 5.8 systematic correction to $H_K(0)$. KOI labeling is the same as in Figure 16 on the right. Lines show predicted loci for 10 Gyr age solar metallicity stars (- - -) and 3 Gyr age metal-poor stars (····) from Dartmouth Stellar Evolution models (Dotter et al. 2008). Note the large number of KOI sub-giants.

based on their KIC values (Batalha et al. 2010). However, significant uncertainty in KIC surface gravities make this selection process suspect. Brown et al. (2011) concluded that uncertainties in KIC log(g) are ∼0.4 dex, and are unreliable for distinguishing giants/main-sequence stars for $T_{\rm eff} \gtrsim 5400$ K. Consequently, a significant fraction of *Kepler* target stars are expected to be F and G spectral-type sub-giant stars (Farmer et al. 2013; Gaidos & Mann 2013).

Finally, to argue for the added value of carrying out this astrometry, Figure 18 plots a theoretical H-R diagram (log g versus log T) for the astrometric reference stars (gray dots) and the Table 4 KOI. The log g and T values are from the *Kepler* Target Search results tabulated at the STScI MAST.[7] There are very few stars in the expected locus of F–G sub-giants. P. A. Cargile et al. (in preparation) have re-measured $T_{\rm eff}$ and log g for 850 KOIs using Keck HiRes archived material and they find a sub-giant fraction among *Kepler* targets similar to that shown in Figure 17. Again, in this plot we include a range of metallicities and ages from the Dartmouth evolution models.

7. SUMMARY

1. Astrometry carried out on *Kepler* data yields significant systematics in position. These systematics correlate with time.
2. Astrometric performance correlates with *Kepler* telescope temperature variations. Larger variations result in poorer astrometry.
3. Astrometric modeling with a previously successful Schmidt model of more than one *Kepler* season fails to produce astrometric precision allowing for the measurement of stellar parallax.
4. Combining *Kepler* astrometry for a single season and channel and three quarters with existing catalog positions and proper motions extends the time baseline to over 12 yr.

[7] http://archive.stsci.edu/kepler/kepler_fov/search.php

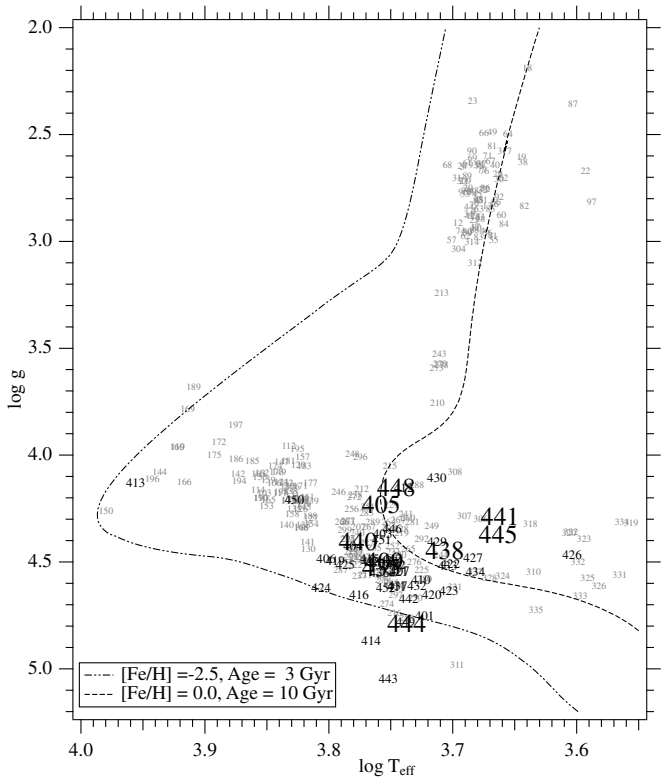

Figure 18. Theoretical H-R diagram for the Section 5.5 astrometric reference stars and the Table 4 KOI. Data are from the MAST. KOI labeling is the same as in Figure 17. The main sequence and giant branch are apparent. Lines show the predicted loci for 10 Gyr age solar metallicity stars (- - -) and 3 Gyr age metal-poor stars (----) from Dartmouth Stellar Evolution models (Dotter et al. 2008). Compared with Figure 17, existing log g values apparently do not readily identify sub-giants.

This provides a mapping of the lower-spatial frequency distortions over a channel, and improves the precision of measured proper motions to 1.0 mas yr^{-1}, over a factor of three better than UCAC4 and PPMXL.

5. Applying that astrometric model, *Kepler* measurements yield absolute proper motions for a number of KOIs with an average proper-motion vector error of $\sigma_\mu = 2.3$ mas yr^{-1}, or $\sigma_\mu/\mu = 19.4\%$. In contrast, averaging the UCAC4 and PPMXL catalog proper motions provides $\sigma_\mu = 5.0$ mas yr^{-1}, or $\sigma_\mu/\mu = 43.0\%$.
6. An RPM diagram constructed from the proper motions determined by our method, when compared to one based on *HST* proper motions, shows a systematic offset. Much of the offset can be attributed to the effect of Galactic rotation on proper motions.
7. The corrected RPM parameter, $H_K(0)$, transformed to $M_K(0)$ through an $H_K(0)$–$M_K(0)$ relation derived from *HST* proper motions and parallaxes, yields $M_K(0)$ for 50 KOIs, including 9 stars with confirmed planetary companions, 8 now confirmed as dwarfs, and 1 a possible sub-dwarf. Six KOIs are identified as giants or sub-giants.

The next significant improvement in KOI proper motions will come from the space-based, all-sky astrometry mission *Gaia* (Lindegren et al. 2008) with ~20 μs of arc precision proper motions and parallaxes for the brighter KOIs. With parallax there will be no need for RPM diagrams. Final *Gaia* results are expected early in the next decade.

This paper includes data collected by the *Kepler* mission. Funding for *Kepler* is provided by the NASA Science Mission directorate. All of the *Kepler* data presented in this paper were obtained from the Mikulski Archive for Space Telescopes (MAST) at the Space Telescope Science Institute (STScI). STScI is operated by the Association of Universities for Research in Astronomy, Inc., under NASA contract NAS5-26555. Support for MAST for non-*HST* data is provided by the NASA Office of Space Science via grant NNX13AC07G and by other grants and contracts. Direct support for this work was provided to G.F.B. by NASA through grant NNX13AC22G. Direct support for this work was provided to A.M.T. by NASA through grant NNX12AF76G. P.A.C. acknowledges NSF Astronomy and Astrophysics grant AST-1109612. This publication makes use of data products from the Two Micron All Sky Survey, which is a joint project of the University of Massachusetts and the Infrared Processing and Analysis Center/California Institute of Technology, funded by NASA and the NSF. This research has made use of the SIMBAD and Vizier databases and Aladin, operated at CDS, Strasbourg, France; the NASA/IPAC Extragalactic Database (NED) which is operated by JPL, California Institute of Technology, under contract with the NASA; and NASA's Astrophysics Data System Abstract Service. This research has made use of the NASA Exoplanet Archive, which is operated by the California Institute of Technology, under contract with the National Aeronautics and Space Administration under the Exoplanet Exploration Program. Some of the data presented herein were obtained at the W. M. Keck Observatory, which is operated as a scientific partnership among the California Institute of Technology, the University of California, and the National Aeronautics and Space Administration. The Observatory was made possible by the generous financial support of the W. M. Keck Foundation. The authors recognize and acknowledge the very significant cultural role and reverence that the summit of Mauna Kea has always had within the indigenous Hawaiian community. We are most fortunate to have the opportunity to conduct observations from this mountain. G.F.B. thanks Bill Jefferys, Tom Harrison, and Barbara McArthur who, over many years, contributed to the techniques reported in this paper. G.F.B. and A.M.T. thank Dave Monet for several stimulating discussions that should have warned us off from this project, but did not. G.F.B. thanks Debra Winegarten for her able assistance, allowing progress on this project. We thank an anonymous referee for a thorough, careful, and useful review which materially improved the final paper.

REFERENCES

Abbot, R. I., Mulholland, J. D., & Shelus, P. J. 1975, AJ, 80, 723
Barclay, T. 2011, Kepler Data Release 12 Notes, Tech. Rep. KSCI-19052-001 (Moffett Field, CA: NASA Ames)
Bastien, F. A., Stassun, K. G., Basri, G., et al. 2013, Natur, 500, 427
Batalha, N. M., Borucki, W. J., Koch, D. G., et al. 2010, ApJL, 713, L109
Bean, J. L., McArthur, B. E., Benedict, G. F., et al. 2007, AJ, 134, 749
Benedict, G. F., McArthur, B., Chappell, D. W., et al. 1999, AJ, 118, 1086
Benedict, G. F., McArthur, B. E., Feast, M. W., et al. 2007, AJ, 133, 1810
Benedict, G. F., McArthur, B. E., Feast, M. W., et al. 2011, AJ, 142, 187
Benedict, G. F., McArthur, B. E., Franz, O. G., et al. 2000a, AJ, 119, 2382
Benedict, G. F., McArthur, B. E., Franz, O. G., et al. 2000b, AJ, 120, 1106
Benedict, G. F., McArthur, B. E., Fredrick, L. W., et al. 2002, AJ, 124, 1695
Benedict, G. F., McArthur, B. E., Gatewood, G., et al. 2006, AJ, 132, 2206
Benedict, G. F., McArthur, B. E., Napiwotzki, R., et al. 2009, AJ, 138, 1969
Benedict, G. F., Shelus, P. J., & Mulholland, J. D. 1978, AJ, 83, 999
Borucki, W. J., Koch, D., Basri, G., et al. 2010, Sci, 327, 977
Brown, T. M., Latham, D. W., Everett, M. E., et al. 2011, AJ, 142, 112
Bryson, S. T., Tenenbaum, P., Jenkins, J. M., et al. 2010, ApJL, 713, L97

Caldwell, D. A., Kolodziejczak, J. J., Van Cleve, J. E., et al. 2010a, ApJL, 713, L92
Caldwell, D. A., van Cleve, J. E., Jenkins, J. M., et al. 2010b, Proc. SPIE, 7731, 773117
Cox, A. N. 2000, Allen's Astrophysical Quantities (4th ed.; New York: AIP)
Dotter, A., Chaboyer, B., Jevremović, D., et al. 2008, ApJS, 178, 89
Farmer, R., Kolb, U., & Norton, A. J. 2013, MNRAS, 433, 1133
Fraquelli, D., & Thompson, S. E. 2012, Kepler Archive Manual (Baltimore, MD: STScI)
Gaidos, E., & Mann, A. W. 2013, ApJ, 762, 41
Gould, A. 2004, arXiv:astro-ph/0403506
Gould, A., & Morgan, C. W. 2003, ApJ, 585, 1056
Harrison, T. E., Bornak, J., McArthur, B. E., et al. 2013, ApJ, 767, 7
Ivezic, Z., Tyson, J. A., Acosta, E., et al. 2008, arXiv:0508.2366
Jefferys, W. H., Fitzpatrick, M. J., & McArthur, B. E. 1988, CeMec, 41, 39
Johansson, E. M., van Dam, M. A., Stomski, P. J., et al. 2008, Proc. SPIE, 7015, 70153
Kozhurina-Platais, V., Sirianni, M., & Chiaberge, M. 2008, in IAU Symp. 248, A Giant Step: From Milli- to Micro-Arcsecond Astrometry, ed. W. J. Jin, I. Platais, & M. A. C. Perryman (Cambridge: Cambridge Univ. Press), 272
Lindegren, L., Babusiaux, C., Bailer-Jones, C., et al. 2008, in IAU Symp. 248, A Giant Step: From Milli- to Micro-Arcsecond Astrometry, ed. W. J. Jin, I. Platais, & M. A. C. Perryman (Cambridge: Cambridge Univ. Press), 217
Malmquist, K. G., & Hufnagel, L. 1933, StoAn, 11, 9
Marcy, G. W., Isaacson, H., Howard, A. W., et al. 2014, ApJS, 210, 20
Martioli, E., McArthur, B. E., Benedict, G. F., et al. 2010, ApJ, 708, 625
McArthur, B. E., Benedict, G. F., Barnes, R., et al. 2010, ApJ, 715, 1203
McArthur, B. E., Benedict, G. F., Harrison, T. E., et al. 2011, AJ, 141, 172
McArthur, B. E., Benedict, G. F., Henry, G. W., et al. 2014, ApJ, 795, 41
McArthur, B. E., Benedict, G. F., Lee, J., et al. 2001, ApJ, 560, 907
Quintana, E. V., Jenkins, J. M., Clarke, B. D., et al. 2010, Proc. SPIE, 7740, 77401
Roelofs, G. H. A., Groot, P. J., Benedict, G. F., et al. 2007, ApJ, 666, 1174
Roeser, S., Demleitner, M., & Schilbach, E. 2010, AJ, 139, 2440
Rowe, J. F., Bryson, S. T., Marcy, G. W., et al. 2014, ApJ, 784, 45
Schlegel, D. J., Finkbeiner, D. P., & Davis, M. 1998, ApJ, 500, 525
Skrutskie, M. F., Cutri, R. M., Stiening, R., et al. 2006, AJ, 131, 1163
Soderblom, D. R., Nelan, E., Benedict, G. F., et al. 2005, AJ, 129, 1616
Steffen, J. H., Fabrycky, D. C., Ford, E. B., et al. 2012, MNRAS, 421, 2342
Stromberg, G. 1939, ApJ, 89, 10
Tanner, A. M., Gelino, C. R., & Law, N. M. 2010, PASP, 122, 1195
Tenenbaum, P., & Jenkins, J. M. 2010, Proc. SPIE, 7740, 7740O
van Altena, W. F. 2013, Astrometry for Astrophysics (Cambridge: Cambridge Univ. Press)
van Cleve, J. E., & Caldwell, D. 2009, Kepler Instrument Handbook, Tech. Rep. KSCI-19033-001 (Moffett Field, CA: NASA Ames)
van de Kamp, P. 1967, Principles of Astrometry (San Francisco, CA: Freeman)
van Leeuwen, F. 2007, *Hipparcos*, the New Reduction of the Raw Data (Astrophysics and Space Science Library, Vol. 350; Berlin: Springer)
Vityazev, V. V., & Tsvetkov, A. S. 2013, AN, 334, 760
Wizinowich, P. L., Le Mignant, D., Bouchez, A., et al. 2004, Proc. SPIE, 5490, 1
Zacharias, N., Finch, C. T., Girard, T. M., et al. 2013, AJ, 145, 44